AGU ADVANCING EARTH AND SPACE SCIENCES

JGR Oceans

RESEARCH ARTICLE

10.1029/2025JC022650

Obliquely Incident Nonlinear Internal Waves on a Shallow Shelf

Christos E. Papoutsellis[1,2], Andrew J. Lucas[1,3], Isha Shukla[1], Kevin M. Okun[3], Robert Pinkel[3], and Oliver T. Schmidt[1]

[1]Department of Mechanical and Aerospace Engineering, University of California, San Diego, CA, USA, [2]Now at Laboratoire d'Hydraulique Saint-Venant EDF R&D, École Nationale des Ponts et Chaussées, Institut Polytechnique de Paris, Chatou, France & Computational Science Research Center at San Diego State University, San Diego, CA, USA, [3]Scripps Institution of Oceanography, University of California, San Diego, CA, USA

Key Points:

- A new statistical space-time framework reveals speed, period, tidal modulation, and angle of incidence of shoaling internal wave events
- 3D simulations and observations suggest that the bottom signatures arise from bolus formation via a fission process during wave shoaling
- Oblique incidence drives along-crest flow and vertical shear feeds transverse instabilities and vortices trailing the shoaling bolus

Supporting Information:

Supporting Information may be found in the online version of this article.

Correspondence to:

C. E. Papoutsellis and A. J. Lucas,
christos.papoutsellis@enpc.fr;
ajlucas@ucsd.edu

Citation:

Papoutsellis, C. E., Lucas, A. J., Shukla, I., Okun, K. M., Pinkel, R., & Schmidt, O. T. (2026). Obliquely incident nonlinear internal waves on a shallow shelf. *Journal of Geophysical Research: Oceans*, *131*, e2025JC022650. https://doi.org/10.1029/2025JC022650

Received 7 JUL 2025
Accepted 27 MAR 2026

Author Contributions:

Conceptualization: Christos E. Papoutsellis, Andrew J. Lucas, Oliver T. Schmidt
Data curation: Andrew J. Lucas, Robert Pinkel, Oliver T. Schmidt
Formal analysis: Christos E. Papoutsellis
Funding acquisition: Andrew J. Lucas, Oliver T. Schmidt
Investigation: Christos E. Papoutsellis, Andrew J. Lucas, Oliver T. Schmidt
Methodology: Christos E. Papoutsellis, Andrew J. Lucas, Oliver T. Schmidt
Project administration: Andrew J. Lucas
Resources: Andrew J. Lucas, Oliver T. Schmidt
Software: Christos E. Papoutsellis, Isha Shukla, Kevin M. Okun, Oliver T. Schmidt
Supervision: Andrew J. Lucas, Robert Pinkel, Oliver T. Schmidt
Validation: Christos E. Papoutsellis

Abstract We introduce a new statistical framework that operates directly in space and time to detect shoaling internal waves as seabed temperature structures observed by a fiber optic distributed temperature sensing array deployed in the coastal waters offshore of California. The nonlinear internal wave exhibited a mean shoaling velocity of approximately 0.09 $\pm$ 0.04 m s^{-1}, with the most commonly observed speed near 0.08 m s^{-1}, a mean period of 14 $\pm$ 7 minutes, and arrived at the fiber at an average angle of incidence of 23° $\pm$ 8° relative to shore-normal. This angle is similar to the orientation of the nearby Scripps branch of the La Jolla Canyon, suggesting that the canyon is a generation site. Nonlinear wave events preferentially occurred during specific phases of the background internal tide, clustered around the ebb phase. To investigate the impact of the oblique angle of approach on the dynamics of shoaling, the observations were used as inspiration for a idealized simulation of a shoaling internal wave approaching a slope at an angle. In the simulation, an initial solitary-like depression wave evolved into elevation boluses propagating obliquely to the isobaths, remaining closely attached to the seafloor as they transported cold water upslope. The shoaling bolus both developed an organized along-crest trailing wake and entrained upslope waters in ways that were quantitatively consistent with the observations. The oblique incidence generated vertically sheared along-crest flow, which may contribute to the coherent structures forming in the trailing wake.

Plain Language Summary Internal waves are underwater waves that travel along density layers in the ocean and can carry cold, nutrient-rich water toward the coast. Using a fiber-optic temperature cable placed on the seafloor offshore of California, we developed a new statistical method to identify individual internal waves directly from their moving temperature signatures. These waves typically traveled upslope at about 10 cm/s and approached the shore at an angle of roughly 20°, similar to the orientation of the nearby Scripps branch of the La Jolla submarine canyon, suggesting the role of the canyon in their generation. Wave events occurred preferentially during certain phases of the internal tide, particularly clustering around 'ebb' conditions when the thermocline is depressed near the seafloor. To understand how the angled approach affects shoaling, we simulated an idealized solitary wave moving obliquely over a sloping bottom. The simulated wave transformed into bottom-attached boluses that transported cold water upslope and generated a coherent, organized wake along the wave crest, quantitatively matching the patterns observed in the field. The results show that the oblique incidence of nonlinear internal waves played a central role in the formation of the observation coherent wake structures and in shaping mixing and transport processes in shallow coastal waters.

1. Introduction

Internal waves permeate the stratified ocean, capable of transferring energy hundreds of kilometers from regions of generation to zones where their energy is dissipated (Garrett & Munk, 1979; Helfrich & Melville, 2006). At the continental margin, incident internal waves undergo a dynamic shoaling process, influenced by the seabed slope, water column stratification, and incident wave properties. Shoaling gives rise to a variety of nonlinear wave phenomena, including the transformation of depression waves into elevation waves and the formation of bores and boluses that propagate along the seafloor (Bai et al., 2019; Hosegood et al., 2004; Klymak & Moum, 2003; MacKinnon & Gregg, 2003; McSweeney et al., 2020; Orr & Mignerey, 2003; Sinnett et al., 2018; Walter et al., 2012; Winant, 1974).

Visualization: Christos E. Papoutsellis
Writing – original draft: Christos E. Papoutsellis, Isha Shukla, Kevin M. Okun
Writing – review & editing: Christos E. Papoutsellis, Andrew J. Lucas, Kevin M. Okun, Robert Pinkel, Oliver T. Schmidt

The diversity of nonlinear phenomena at play highlights the complexity and variability of internal wave dynamics in coastal setting, and the challenge of getting comprehensive observations. Given the known importance of internal wave shoaling and breaking processes to vertical mixing and cross-shore transport in coastal waters, coastal geomorphology and exchange of sediments, pollutants, nutrients and larvae in coastal shelf (Cheriton et al., 2014; Davis & Monismith, 2011; Emery & Gunnerson, 1973; Lucas et al., 2011; Omand et al., 2011; Pineda, 1991), new observational techniques need to be developed to answer this challenge. For comprehensive overviews of these processes, see Woodson (2018) and Boegman and Stastna (2019).

The understanding of the internal wave shoaling process has advanced through numerical modeling (Stastna & Legare, 2024; Venayagamoorthy & Fringer, 2012), laboratory experiments (Dauxois et al., 2004; Ghassemi et al., 2022; Hartharn-Evans et al., 2022; Michallet & Ivey, 1999; Wallace & Wilkinson, 1988), and field observations, with recent work capturing significant seafloor temperature variations during wave shoaling using high spatio-temporal resolution fiber optic distributed temperature sensing (DTS) (Davis et al., 2020; Lucas & Pinkel, 2022; Sinnett et al., 2020). In particular, Lucas and Pinkel (2022) demonstrated that the shoaling process at the coast of La Jolla is highly nonlinear and three-dimensional, characterized primarily by long-crested internal-wave structures propagating onshore with periods on the order of tens of minutes and wavelengths 100 m and less. Despite the wealth of observational data, the complexity of the seafloor signatures of these shoaling-wave structures often presents challenges for systematically analyzing wave characteristics. Interpreting these complex signatures and connecting them to the underlying wave dynamics is a challenge that we address in this work.

Three-dimensional (3D) simulations in realistic domains can capture internal-wave dynamics undergoing shoaling and breaking but require substantial computational resources. Nonetheless, laboratory-scale high-fidelity simulations have elucidated the shoaling process and the nonlinear instabilities which can occur, for example, Arthur and Fringer (2016); Xu and Stastna (2020); Vieira and Allshouse (2020). For a recent review and an up-to-date bibliography see Stastna and Legare (2024). In particular, Aghsaee et al. (2010) classified different types of internal wave breaking over constant-slope bathymetry, while Xu and Stastna (2020) demonstrated that shoaling depression waves on mild slopes can generate bottom-attached separation bubbles during fission. Complementing these studies, large-scale numerical models with parameterized subgrid-scale vertical mixing have been used to study shoaling internal wave dynamics. These models are essential for studying realistic scenarios where high-resolution methods are computationally prohibitive, enabling insights into shoaling processes in coastal environments. For example, Vlasenko and Stashchuk (2007) demonstrated wave refraction over strong three-dimensional bottom variations, Guo et al. (2021) investigated particle transport during shoaling, and Dauhajre et al. (2021) investigated how the vertical stratification structure influences two-dimensional bore propagation over a gentle slope. The present work builds on these efforts by studying shoaling waves observed offshore of La Jolla, California, with a combination of seabed temperature measurements from a distributed fiber optic temperature sensing system and 3D non-hydrostatic numerical modeling.

The observational data considered in this work document internal wave trains shoaling at the La Jolla coast from June 25 to 23 August 2013 (Lucas & Pinkel, 2022). The seafloor temperature signature of these waves was captured through an L-shaped fiber optic array, with legs positioned in the cross-shore and alongshore directions of the bathymetry. The DTS array consisted of a 460 m cross-shore leg and a 1,000 m alongshore leg, denoted as C and A respectively, in Figure 1a. The seafloor temperature observations were produced with a 0.5 m spatial and a 20 s temporal averaging along a 1.5 km cable for a period of 2 months. The observations were calibrated to in situ thermistors as described in Sinnett et al. (2020), yielding a ± 0.05°C and ± 0.1°C accuracy for the spatiotemporal averaging stated above. Given the exceptionally strong temperature gradients in the thermocline during the study period, this precision was easily capable of tracking the seabed temperature signals associated with the shoaling waves. More detailed specifications can be found in Lucas and Pinkel (2022) and fiber optic DTS for oceanographic applications is described in Sinnett et al. (2020).

A typical spacetime plot of the seafloor temperature is presented in Figure 1b. The cross-shore signature revealed the final stages of bottom-attached cold-water packets propagating up the slope into warmer water for several hundred meters. The alongshore signature indicated that these packets were long-crested, extending coherently for approximately 1 km in the alongshore direction, see Figure 1 and (Lucas & Pinkel, 2022, Figure 6). These signatures also indicate that, inshore of the 35 m isobath, the wave trains captured by the bottom array C arrive in groups of individual long crested waves (Lucas & Pinkel, 2022). As noted in this paper, the signature of the waves within about 100 m of the crossing of the alongshore and cross shore cables suggests that waves intersect the

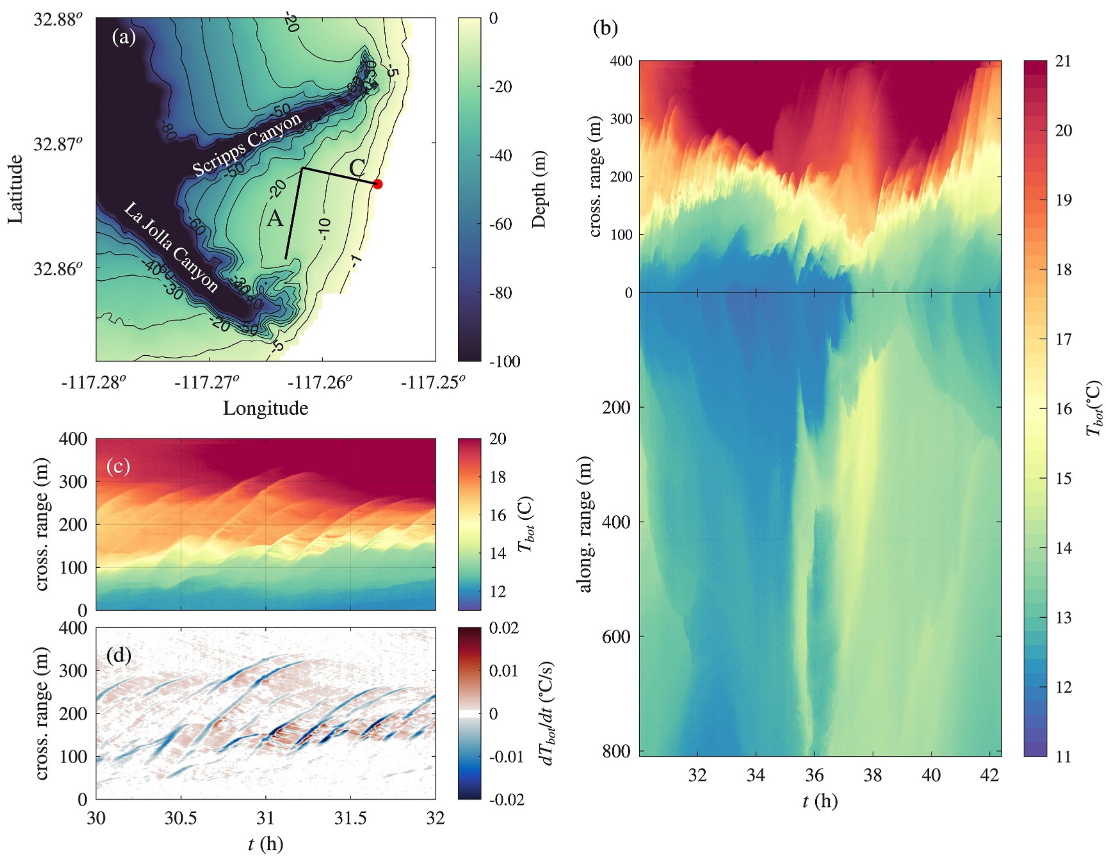

Figure 1. (a) The coastal bathymetry of the region of interest with the Scripps and La Jolla canyons. The straight black lines represent the cross and alongshore optical cables denoted by C and A, respectively. The red dot represents the Scripps pier. (b) Typical space-time plots of seafloor temperature T_{bot} along the cross-shore and alongshore cables. The cross-shore range increases toward the Scripps pier. The alongshore range increases away of the cable bend. (c) Close-up view of the seafloor temperature, corresponding to the first 2 hours shown in panel (b). (d) The rate of change of the cross-shore signal, dT_{bot}/dt, corresponding to panel (c).

alongshore cable A at its north end first, suggesting a north-to-south propagation pattern along the cable. Moreover, the wave crests are not aligned purely in the along-shore direction as they approach the coast. These trajectories become more apparent when examining the rate of change of the seafloor temperature, dT_{bot}/dt. Figures 1c and 1d provide close-up views of T_{bot} and dT_{bot}/dt, respectively. The trajectories of the onshore propagating wave structures correspond to bands of negative dT_{bot}/dt. Adjacent to this bands, we observe smaller bands of positive dT_{bot}/dt directed offshore. This pattern suggests the presence of trailing temperature oscillations following the main shoaling structure, as described by Lucas and Pinkel (2022). Notably, the signal also displays trajectories that appear to overtake or intersect one another, forming a characteristic inverted-Y pattern. For an additional example of this phenomenon, see (Lucas & Pinkel, 2022, Figure 6). While these internal wave signatures were distinctive and coherent, their spatial and temporal variability complicates their analysis.

The present study addresses this challenge in two ways. First, we introduce a method that directly analyzes spatio-temporal onshore trajectories to detect shoaling events and extract key wave characteristics, specifically propagation velocities, periods, and angle of approach, as well as the phase relationship between shoaling internal waves and the background tidal flow. Second, we employ idealized non-hydrostatic simulations to investigate the shoaling process and its role in shaping the observed signatures.

The structure of the paper is as follows: Section 2 examines the available observational data on the seafloor signature and introduces a new technique for identifying the seafloor signature of shoaling nonlinear internal waves. A statistical analysis of the dominant speeds, periods, and frequency of occurrence during a tidal cycle is presented. Section 3 details the numerical model and presents the results, emphasizing the relationship between seafloor temperature and the underlying internal wave dynamics. Finally, a discussion of our findings is presented in Section 4.

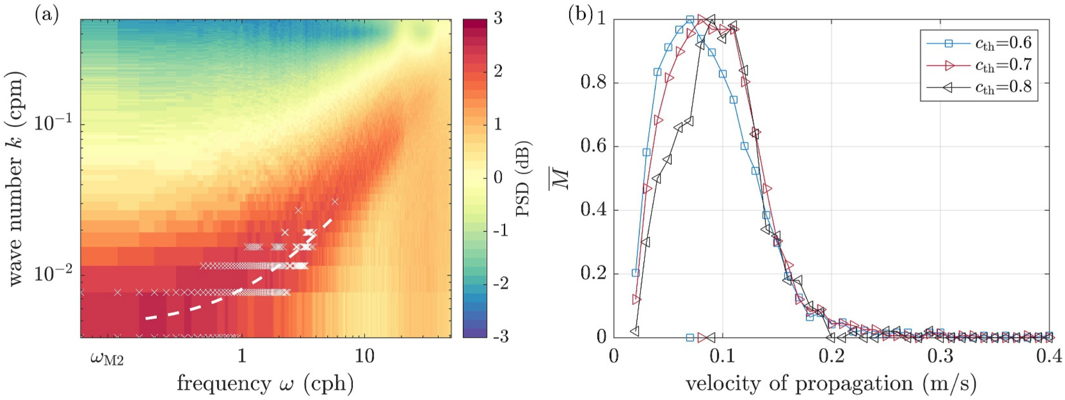

Figure 2. (a) Power spectral density (PSD) in log-log scale calculated from data collected by the cross-shore cable over a period of 19 consecutive days. Frequency ω and wave number k are expressed in cycles per hour (cph) and cycles per meter (cpm), respectively. Only the domain corresponding to positive wave numbers is shown. $\omega_{M2} = 0.08$ cph is the frequency of the M_2 tide. The white crosses represent the (ω, k) points corresponding to the top 60% of the PSD. The white dashed line is obtained by linear interpolation of this points and represents a constant velocity, $v_{p,c} = 0.08$ m/s. (b) Normalized count number $\overline{M}$ as a function of the propagation velocity $v_{p,c}$ for different values of the threshold c_{th}. The markers on the horizontal axis indicate the velocity propagation at maximum $\overline{M}$.

2. Seafloor Signatures of Shoaling Internal Waves

We analyze the signal captured by the cross-shore cable during a 19-day period from July 11th to 30th when shoaling activity was particularly intense. We shall first consider the Power Spectral Density (PSD) across the wave number-frequency domain. The PSD calculation utilizes the rate of change of seafloor temperature data, dT_{bot}/dt, as a function of space and time, which acts as a prewhitening step by reducing large-scale variability and enhancing wave-induced variability. Observations are broken into overlapping segments of duration equal to one M_2 tidal cycle (12.42 hr), with an overlapping coefficient of 0.5, and are treated with a Hamming window. A two-dimensional Fast Fourier Transform (2DFFT) is then performed for each time segment across the entire spatial range (Lucas & Pinkel, 2022).

To highlight the wave number structure of frequencies higher than tidal, we normalize the frequency-wave number spectra by dividing the PSD at each frequency $S(k, \sigma)$ by the average PSD across all wave numbers at that frequency. This normalized PSD is expressed as,

$$\mathrm{PSD} = \frac{S(k, \sigma)}{\frac{1}{n}\sum_{k_0}^{k_n} S(k, \sigma)}, \tag{1}$$

where k is the wave number with a subscript n referring to the resolved wave number bands. We show the PSD in Figure 2 on a logarithmic scale. We recall from Lucas and Pinkel (2022) that the energy is onshore-polarized, particularly in the high frequency-wave number region demonstrating that most energy is dissipated over the inner shelf, rather than reflected back offshore. If we select the (ω, k) region corresponding to the top 60% of the maximum PSD (white crosses in Figure 2a), we observe that this region is mostly concentrated around a straight line corresponding to a specific propagation velocity. A linear fit on the (ω, k) points of this region leads to a value of approximately 0.08 m/s. This suggests the presence of energetic wave activity corresponding to this propagation velocity. This frequency/wavenumber analysis provides important information, but collapses important aspects of the variability of individual events, and their clustering in time. Complementary methodologies have used wavelet transforms to characterize nonstationary internal-wave records (e.g., Davis et al. (2008); Walter et al. (2016)). Here, we employ a time/space domain analysis that can detect these signatures and assess their individual characteristics. In particular, our method is based on space–time cross-correlation, which yields automated event detection and identification of propagation speeds. In this sense, it complements the event-by-event wavefront fitting of Lucas and Pinkel (2022) which becomes less practical when events are numerous. Moreover, it is conceptually related to the matched filter approach of Colosi et al. (2018).

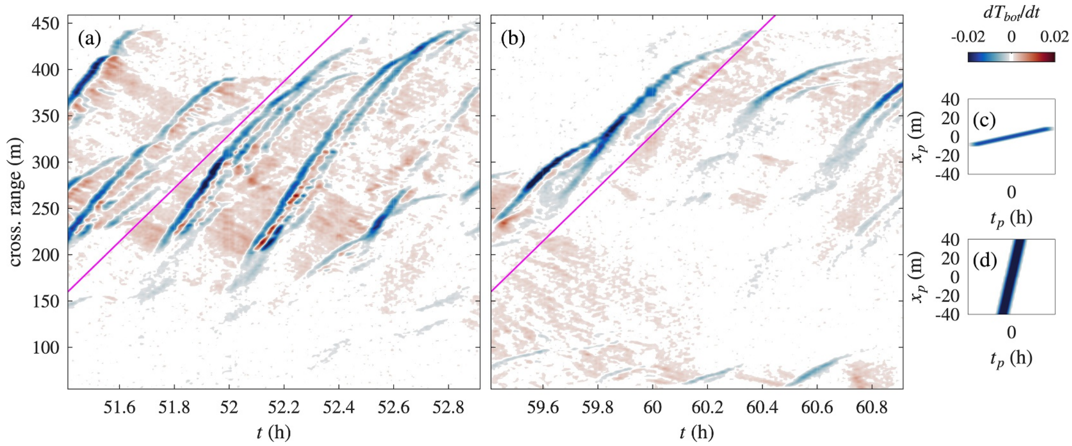

Figure 3. Rate of change dT_{bot}/dt (in C°/s) for the cross-shore distributed temperature sensing cable for two different 1.5-hr intervals ((a) and (b)). Cross-shore range is increasing toward the Scripps Pier. The magenta line corresponds to a trajectory with propagation velocity $v_{p,c} = 0.08$ m/s. The panels at the right display two of the prototypes used in the data analysis, corresponding to propagation velocities 0.02 m/s and 0.4 m/s, respectively.

2.1. Wave Event Detection

Our analysis focuses on the detection of seafloor temperature structures, which facilitates the quantification of various properties of the shoaling waves. A small sample of the data used in this analysis are shown in Figures 3a and 3b. The samples show the existence of space-time trajectories with varying propagation speeds (blue bands) extending over cross-shore length scales of 50–300 m and with durations that can last up to one hour. These cold water features are footprints of individual wave structures propagating onshore (Lucas & Pinkel, 2022). The slope of each individual space-time trajectory is indicative of the onshore velocity component of the wave structure as it propagates up the bathymetric slope.

Our objective is to detect and classify signatures of onshore propagating wave structures as the ones illustrated in Figures 3a and 3b with respect to their velocities of propagation. To this end, we use a technique based on the cross-correlation of the observed data sets with prototypical spatio-temporal signatures corresponding to constant propagation velocities.

First, we construct generic prototypes resembling a single band in the observed data set. Each prototype is generated by defining a Gaussian profile in time, based on the shape of a typical observed feature. This Gaussian profile is centered and extended along a straight line segment whose slope determines the prototype velocity, creating a set of prototypical bands. These prototypical bands are confined within a spatio-temporal domain, D, extending 1,000 s in time and 80 m in the cross-shore direction and correspond to velocities of propagation that lie within the range $v_{p,c} \in [0.02{:}\ 0.01{:}\ 0.4]$ m/s. D was chosen to be large enough to avoid detecting very short, poorly developed tracks, yet compact enough to preserve prototype fidelity for approximately straight, well-developed tracks. The prototypical bands corresponding to the extremities of this interval are shown in Figures 3c and 3d.

For every prototype, we calculate the normalized cross-correlation with the data set generating a cross-correlation coefficient in the spatio-temporal domain with values within a range of ± 1. Regions in the data that closely resemble a prototype correspond to a large positive cross-correlation coefficient value. We consider that an event corresponding to a given propagation velocity or prototype has been identified if the cross-correlation coefficient obtained from this prototype exceeds a threshold value c_{th}. To ensure that the identified space-time locations exceeding the threshold do not correspond to the same signature, we apply a process to exclude overlapping detected regions in space and time. This is achieved by systematically checking for overlaps between detected regions and retaining only the highest cross-correlation coefficient within each overlapping area. By doing so, we eliminate redundant detections and ensure that each signature is represented uniquely within the spatio-temporal domain. We can then count the number of detections $M(v_{p,c})$ corresponding to every prototypical onshore velocity, $v_{p,c}$, to generate a distribution of the number of detections. Results on the normalized count number

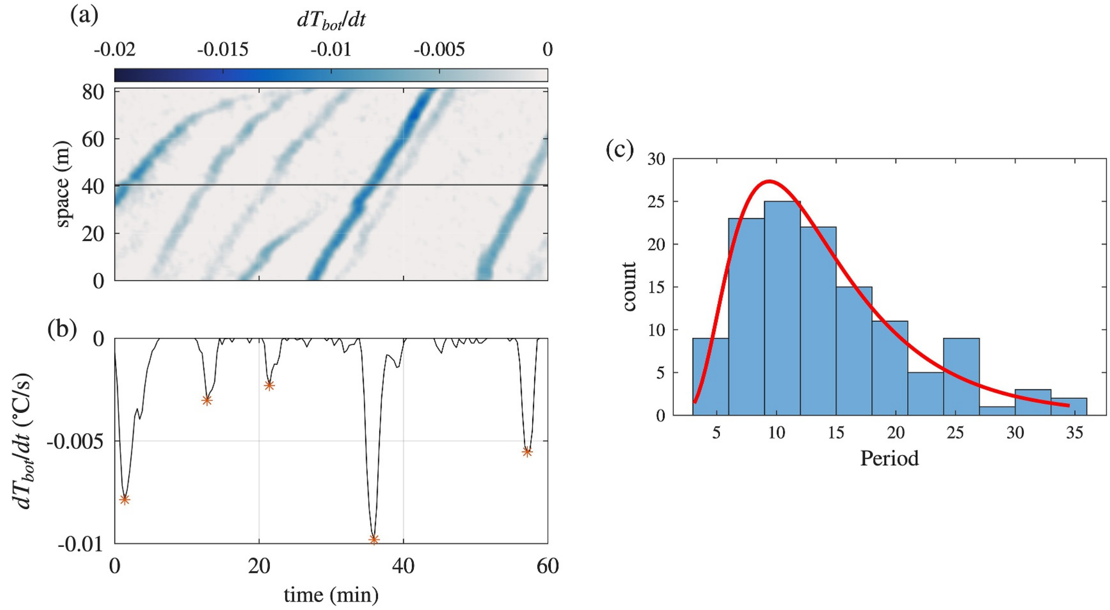

Figure 4. (a) Space-time plot of the negative part of dT_{bot}/dt for a region spanning over 60 min in time and 80 m in space enclosing an identified event with $v_{p,c} = 0.08$ m/s (b) Time series of the negative part of dT_{bot}/dt evaluated along the spatial position corresponding to 40 m (indicated by the black line in panel (a)). (c) Histogram of the calculated periods with an overlaid (scaled) Inverse Gaussian fit (red line). The mean and shape parameters of the fitted distribution are $\mu = 14.2$ min and $\lambda = 50.8$ min, respectively and the peak period is 9.4 min.

$\overline{M} = M(v_{p,c})/\max\{M(v_{p,c})\}$ for different values of the threshold c_{th} ($c_{\mathrm{th}} = 0.6, 0.7, 0.8$) are shown in Figure 2b. For $c_{\mathrm{th}} = 0.6$, $\overline{M}$ is increasing rapidly with increasing $v_{p,c}$ up to $v_{p,c} = 0.07$ m/s where it reaches a maximum size. Beyond $v_{p,c} = 0.07$ m/s, $\overline{M}$ decreases rapidly until $v_{p,c}$ exceeds 0.15 m/s, after which the decrease continues but at a slower rate, indicating that higher velocities occur less frequently in the data set. A similar trend is observed for $c_{\mathrm{th}} = 0.7$ and 0.8, with maxima in $\overline{M}$ occurring at 0.08 and 0.09 m/s, respectively. The weighted mean velocities and standard deviations for the three cases are 0.092 ± 0.048, 0.092 ± 0.042, and 0.098 ± 0.048 m/s, respectively, indicating limited sensitivity to the choice of correlation threshold. Any variation is attributed to differences between the samples and the real signals. Overall, the method consistently identifies the most frequently occurring velocities in the data set as being in the range 0.07–0.09 m/s. These values align with the 2D FFT analysis, which indicates that the energetic region of the spectrum is concentrated around this velocity range. This consistency implies that the dominant wave events, characterized by high energy, correspond to the most frequent wave events observed in the system. For simplicity, we designate $v_{p,c} = 0.08$ m/s as the dominant velocity.

2.2. Estimation of Wave Periods

We continue the analysis to estimate a statistically dominant period for the detected events corresponding to the dominant velocity, taken here to be 0.08 m/s. For every detected event, we search a 60 min window for other wave signatures. An example is shown in Figure 4a. For each of such regions, we extract a time series by evaluating dT_{bot}/dt at the middle of the spatial domain (Figure 4b). We then identify the peaks, and compute the time differences between them. Their mean value provides an estimate of the dominant period for the considered time series (see Figure 4b). This leads to a set of estimated periods. A histogram of these periods is shown in Figure 4c. To characterize the distribution and determine the peak period, we fit an inverse Gaussian distribution (see, e.g., Soomere et al. (2020)), which effectively captures the right-skewed nature of the calculated periods. The fitted distribution has a mean of $\mu = 14.1$ min and a shape parameter of $\lambda = 50.8$ min with a standard deviation $\sigma = 7.5$ min. The peak period is estimated at 9.4 min, indicating that this is the most frequent time difference between trajectories. This value corresponds to a frequency of approximately 6 cycles per hour, which appears to be a persistent feature of the internal-wave shoaling process. Although such high frequencies are visible in the PSD (see Figure 2a), they are not the dominant components in the spectrum. This demonstrates how the proposed

10.1029/2025JC022650

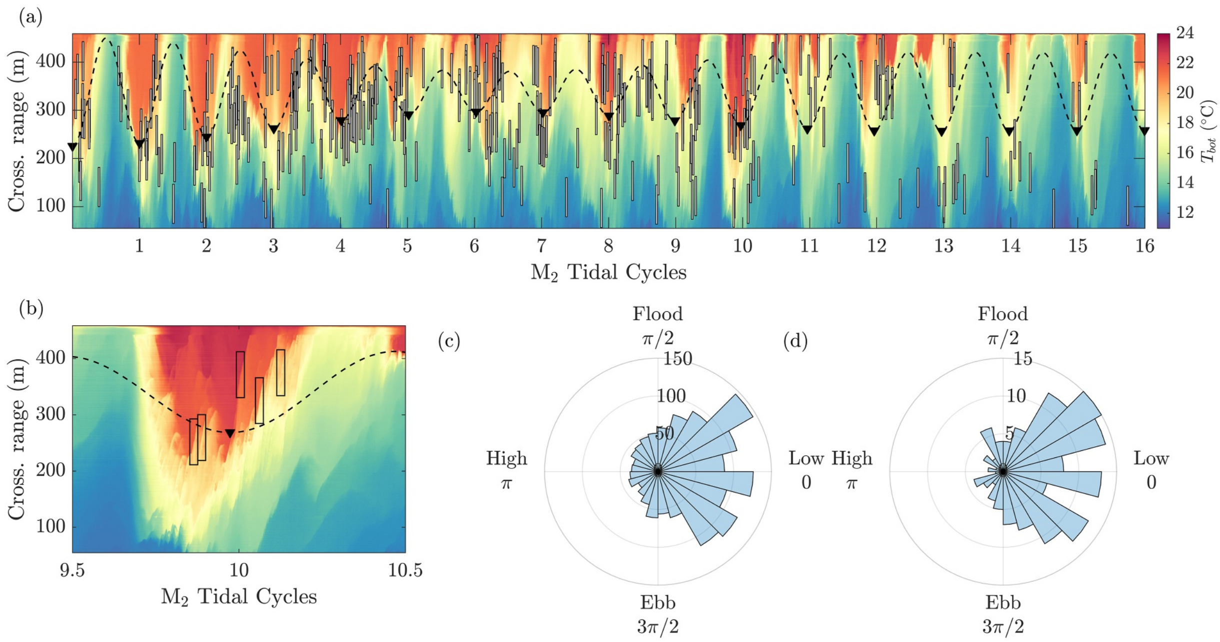

Figure 5. (a) Bottom temperature signal T_{bot} from distributed temperature sensing shown here for 16 of the 36 M_2 tidal cycles analyzed, for clarity. White rectangles correspond to detected events with propagation velocities in the range $v_{p,c} \in [0.04, 0.14]$ m/s. The dashed black line shows the extracted M_2 tidal signal based on the 17 °C isotherm. Black triangles indicate the timing of low tides. (b) Close up view for one tidal cycle. Black rectangles show the detected events with the dominant velocity $v_{p,c} = 0.08$ m/s. (c) Rose diagram of all event occurrences as a function of the tidal phase. (d) Rose diagram for the events corresponding to the dominant velocity of propagation, $v_p = 0.08$ m/s.

analysis complements the 2D FFT by revealing a sustained timing pattern in shoaling events that may not be fully captured in the spectral domain.

2.3. Relationship Between the Internal Tide and Shoaling Event Occurrence

One key advantage of detecting events directly in the space–time signal is the ability to investigate whether these events occur preferentially at certain phases of the internal tidal (M2) cycle.

The first step in this analysis is to extract the tidal signal from the DTS data. To this end, we consider an isotherm in space-time corresponding to $T_{\text{bot}} = 17$ C°, which approximately corresponds to the local thermocline. The resulting signal captures the excursion of the point where the thermocline intersects the bottom slope, effectively tracing the run-up and run-down of the thermocline and providing a means to follow the internal tidal phase.

It is known that the M_2 tide dominates the local internal wave field (Winant, 1974). To isolate this constituent from the signal and to remove any high-frequency variability, we apply a bandpass filter centered at the M_2 frequency ($f_{M_2} = 0.0805$ cph) with a bandwidth of ±0.0075 cph. The timings of the low tide are then identified from the filtered signal. In Figure 5a, we show a portion of the DTS signal used in this analysis along with detected events (corresponding to $c_{\text{th}} = 0.7$) and the filtered tidal signal (dashed line). A close-up is shown in Figure 5b.

With the tidal signal extracted, we can now compute the relative timing of each detected event with respect to the tide. This is done by referencing all event times to a low tide and expressing them as phases within the tidal cycle, $\varphi_i \in [0, 2\pi)$. To analyze the distribution of these phases, we employ circular statistics (Bowers et al., 2000; Fisher, 1995; Kalai & Mondal, 2022). The concentration of detected phases is quantified using the mean resultant vector, $R = 1/N \sum_{i=1}^{N} \exp(\mathrm{i}\varphi_i)$, where N is the number of detections. The mean resultant length, $|R|$, provides a measure of phase concentration, with values close to 1 indicating strong clustering. The argument $\arg R \in [0, 2\pi)$ represents the circular mean direction, that is, the preferred phase within the tidal cycle.

In Figure 5c, we plot the rose diagram of all event detections. In our convention, $\theta = 0$ corresponds to the low tide and the phase increases counterclockwise. The distribution is asymmetric with a large number of events occurring around the low tide, $\theta = 0$. We have $|R| = 0.3$, indicating a moderate phase concentration with a preferred phase

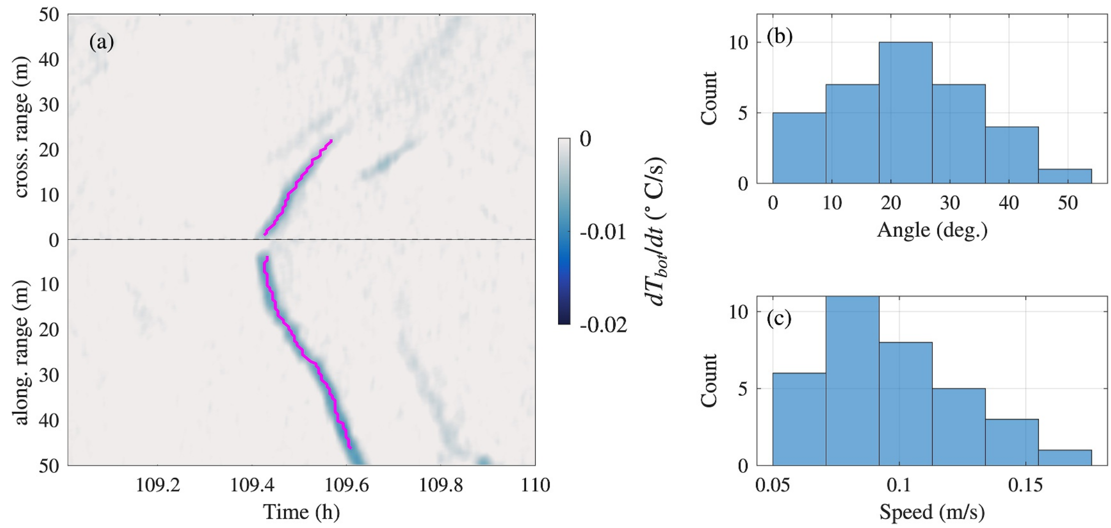

Figure 6. (a) Space-time plot of the negative part of dT_{bot}/dt for one of the 34 identified events exhibiting both cross-shore and alongshore signatures. The domain spans 60 min in time and 50 m in both spatial directions. Magenta lines represent the space-time trajectories. The black dashed line corresponds to the intersection point of the two cables. (b) Histogram of propagation angles and (c) Histogram of velocity magnitudes, computed from all 34 detected events.

angle that aligns almost exactly with low tide, $\arg R = 0.03$. To assess whether events corresponding to the dominant velocity exhibit a clearer tidal phase preference, we consider the distribution of the subset of detections corresponding to $v_p = 0.08$ m/s in Figure 5d. The distribution follows a similar asymmetric trend, with most events occurring during the early flood phase (shortly after the low tide) and the late ebb phase (shortly before the low tide). The mean resultant length is $|R| = 0.40$, indicating a stronger phase concentration with $\arg R = 0.99 \times 2\pi$. The similarity between the two distributions reflects the fact that the largest number of events in panel (c) exhibit propagation velocities in the neighborhood of the dominant value, so the overall phase structure is already shaped by these events. The increased concentration in the distribution of panel (d) highlights the tighter modulation of the dominant events by the internal tide. In general, very few events occur in the range $\varphi \in (\pi/2, 3\pi/2)$ indicating a preferred occurrence near the low tide, or, equivalently, the time when the thermocline reaches its lowest position along the bottom DTS fiber. This preference suggests a form of phase locking to the M_2 tide.

2.4. Estimation of Local Wave Direction

Having identified the shoaling events using the cross-shore fiber, we now examine the signatures captured by the alongshore fiber to infer the direction of wave propagation and the magnitude of the velocity. Among the events detected in the cross-shore fiber, we have isolated 34 cases that exhibit a clear signal in both cross-shore and alongshore directions within 50 m of the cable turn (gray box in Figure 1a). An example of such an event is shown in Figure 6a. Since the two fibers are arranged orthogonally, we can deduce the full velocity vector for each of the 34 events from the cross-shore and alongshore velocity components. Each vector is defined relative to the fiber intersection point, with its origin located at this point and its components determined by the observed displacements in both directions. Note that this interpretation remains consistent in a neighborhood around the intersection point. Here, we restrict our analysis to a 50-m by 50-m region beginning at the fiber intersection.

We extract temporal transects at each spatial location along the fibers, identify the bottom temperature gradient minima within a defined temporal search window, and terminate the trajectory when the signal-to-noise ratio of the minima drops below 25. In this way, we construct the shoaling wave trajectories through space and time along both segments. The propagation angle is then computed using the arctan of the alongshore and cross-shore displacement vectors relative to the fiber intersection point. By convention, positive angles indicate wave approach from the north, while negative angles indicate approach from the south, relative to the cross-shore axis. An angle of 0° corresponds to a vector aligned with the cross-shore direction and pointing onshore, with angles increasing in a clockwise direction.

Panels (b) and (c) present the histogram of the calculated angles and velocity magnitudes corresponding to the 34 detected events. The distribution of propagation angles ranges from approximately 0° to 50°, with a peak near 20°. The distribution is positively skewed and most angles are within 10°–30°. A few events occur at more oblique angles. The mean angle is approximately 23°. The distribution of wave propagation speeds ranges from approximately 0.05 m/s to 0.18 m/s, and is positively skewed, with the most frequent speeds between 0.07 and 0.09 m/s.

3. Simulation of Internal Wave Shoaling Events

The previous analysis provided information regarding the propagation speed, period, phasing, and angle of approach of the seabed cold water signatures. These observations are used as inspiration for an idealized numerical simulation of the shoaling process. The aim of this numerical experiment was two-fold: (a) to ascertain whether the observed shoaling properties, including the trailing wave-wake, could be generated from simple initial offshore conditions, and (b) investigate the role of oblique incidence in the shoaling process.

3.1. Model Setup

We perform our simulations using the non-hydrostatic version of the Massachusetts Institute of Technology general circulation model (MITgcm) (Marshall et al., 1997), which solves the Navier-Stokes equations under the Boussinesq approximation. We assume that temperature is the only active tracer, the equation of state is linear, and the effects of rotation can be neglected. For the bottom boundary condition, a quadratic bottom drag coefficient of $C = 0.003$ is applied, while a linear boundary condition is assumed at the free surface. On the shore, we apply a free-slip boundary condition. At the remaining boundaries, we introduce relaxation zones that absorb incoming waves to avoid unwanted reflections.

The vertical stratification profile is characterized by the three-parameter formula for the Brunt–Väisälä frequency introduced in Vlasenko et al. (2000):

$$N_0(z) = N_{\max}\left(\left[\frac{2(z + H_N)}{L_N}\right]^2 + 1\right)^{-1}, \tag{2}$$

where H_N is the depth where N is maximum ($N(-H_N) = N_{\max}$) and L_N represents a length scale characterizing the vertical variation of N. From (2), we calculate the corresponding unperturbed density profile which, in conjunction with a linear equation of state, leads to the vertical temperature profile needed to initialize the simulations. The parameters in (2) are selected so that the stratification resembles observations offshore of La Jolla. Specifically, $H_N = 19$ m and $N_{\max} = 0.019$ s^{-1} are based on seasonal data from the World Ocean Atlas 2023, and we take $L_N = 20$ m (Locarnini et al., 2024). This serves as our baseline stratification, and we shall also present results for several nearby parameter variations in Section 3.3.

We extract the bathymetry by choosing a straight transect that approximately follows the path of the deployed cross-shore DTS cable from the Scripps Pier to the eastern rim of the Scripps Canyon at a depth $H = 60$ m (Figure 7a). Next, we smooth and extend this bathymetry by a flat region that is used for the placement of the initial condition, and extrude the resulting bathymetry along the transverse direction; see Figure 7b. Consequently, in the present model, the bathymetry varies only in x, the cross-shore direction, while remaining constant in y, the alongshore direction. The slope of the bathymetry is shown in the inset of Figure 7b. It is approximately 15% near the 40 m isobath, gradually decreasing toward the coast, and remaining below 5% beyond the 20 m isobath. The mean slope is approximately 0.024. For a typical depression wave with an amplitude of 8 m and a wavelength of 150 m, we obtain an Iribarren number of approximately 0.1.

To initialize our simulations, we generate the initial conditions for the horizontal velocities (u, v) and the temperature T using a solitary wave solution of the Dubreil-Jacotin-Long (DJL) equation. The DJL equation is the steady-wave version of the two-dimensional governing equations for an incompressible, inviscid fluid under the Boussinesq approximation and a rigid lid assumption (Turkington et al., 1991). The DJL solution provides a fully nonlinear, steady wave that avoids both the early adjustment seen when starting from weakly nonlinear theories and the associated vertical-structure discrepancies, see Vlasenko et al. (2000). To construct our three-dimensional initial conditions for the above stratification, we first calculate the velocity and temperature fields of a two-

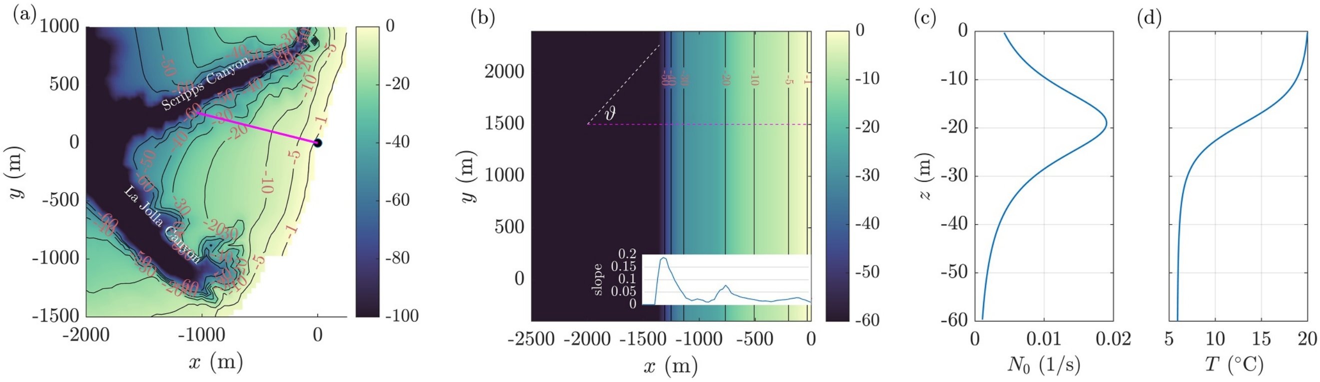

Figure 7. (a) The La Jolla bathymetry from pv-lab.org/ncex. The magenta line represents the path of the cross-shore cable. (b) Two-dimensional bathymetry in three dimensions used in the simulation. The white dashed line represents the crest of the initial solitary-like depression wave and the magenta dashed line the cross-shore direction in the computational domain. The inset shows the slope of the bathymetry in the x-direction. (c) Brunt–Väisälä frequency, Equation 2, with $H_N = 19$ m, $L_N = 20$ m and $N_{\max} = 0.019$ 1/s. (d) Unperturbed vertical temperature profile.

dimensional (2D) solitary wave of depression at depth $H = 60$ m using the MATLAB code provided in Dunphy et al. (2011). In our basic simulation, the initial depression solitary wave has an amplitude of 8 m and a offshore phase speed of 0.25 m/s, consistent with observations of these small amplitude waves in the area (Lucas & Pinkel, 2022). Once the solitary wave is computed, we extend the 2D solitary wave fields in the transverse direction to construct a long-crested solitary wave, which is uniform along the direction perpendicular to its propagation direction. Next, we multiply the resulting fields by an envelope tanh function that causes them to rapidly decay after a length $L \approx 1$ km. We further assume that a generation source of internal waves in the region of interest is the Scripps Canyon, and that the initial propagation direction is oriented perpendicular to its axis. To accommodate for this oblique approach to shore, the initial conditions are rotated at an angle ϑ with respect to the direction normal to the shore and then interpolated on the computational grid. Here, we choose $\vartheta = 40°$, a value that represents the angle that the Scripps Canyon makes with respect to the cross-shore direction, see Figure 7(b). We note that observations indicate a smaller mean local angle ($\approx 23°$) in the shoaling region, suggesting that wave propagation undergoes refraction (see Section 3.2.1); here we prescribe the offshore incidence angle based on canyon geometry.

To model the anticipated turbulence and mixing during the shoaling process, we employ the Richardson-number-dependent parametrization introduced in Pacanowski and Philander (1981), PP81. This approach models the influence of unresolved subgrid-scale processes that cannot be explicitly represented at our simulation scale. In the PP81 scheme, the vertical viscosity ν and diffusivity κ are calculated by

$$\nu = \frac{\nu_0}{(1+\alpha \mathrm{Ri})^n} + \nu_b, \quad \kappa = \frac{\nu}{(1+\alpha \mathrm{Ri})} + \kappa_b. \tag{3}$$

In (3), the Richardson number is given by $\mathrm{Ri} = N^2/\left(u_z^2 + v_z^2\right)$ where u, v denote the horizontal velocity fields and u_z, v_z their vertical derivatives, and ν_b and κ_b denote constant background viscosity and diffusivity coefficients, respectively. The parameters α and n are set to $\alpha = 5$ and $n = 1$ as in Vlasenko and Stashchuk (2007); Guo et al. (2021); He et al. (2023). The background values are $\nu_b = 10^{-5}$ m^2/s^{-1} and $\kappa_b = 10^{-5}$ m^2/s^{-1}, and $\nu_0 = 2 \times 10^{-3}$ m^2/s^{-1}.

Horizontal diffusivity and viscosity are $\nu_h = 10^{-4}$ m^2/s^{-1} and $\kappa_h = 10^{-5}$ m^2/s^{-1}, respectively, with an additional contribution to the viscosity from a Smagorinsky-type parametrization using a coefficient of 0.3. The spacing of the horizontal grid is $(\delta x, \delta y) = (2.39, 2.54)$ m in the main computational domain and increases exponentially in the relaxation zones which extend over 18 grid points, up to (300,305) m. In the vertical direction, we use a non-uniform grid that increases resolution near the sea surface from 0.86 to 0.26 m. The total number of cells is $900 \times 900 \times 100 = 81 \times 10^6$. The time step is 0.5 s, and we let the simulation run for 5.2 hr of physical time.

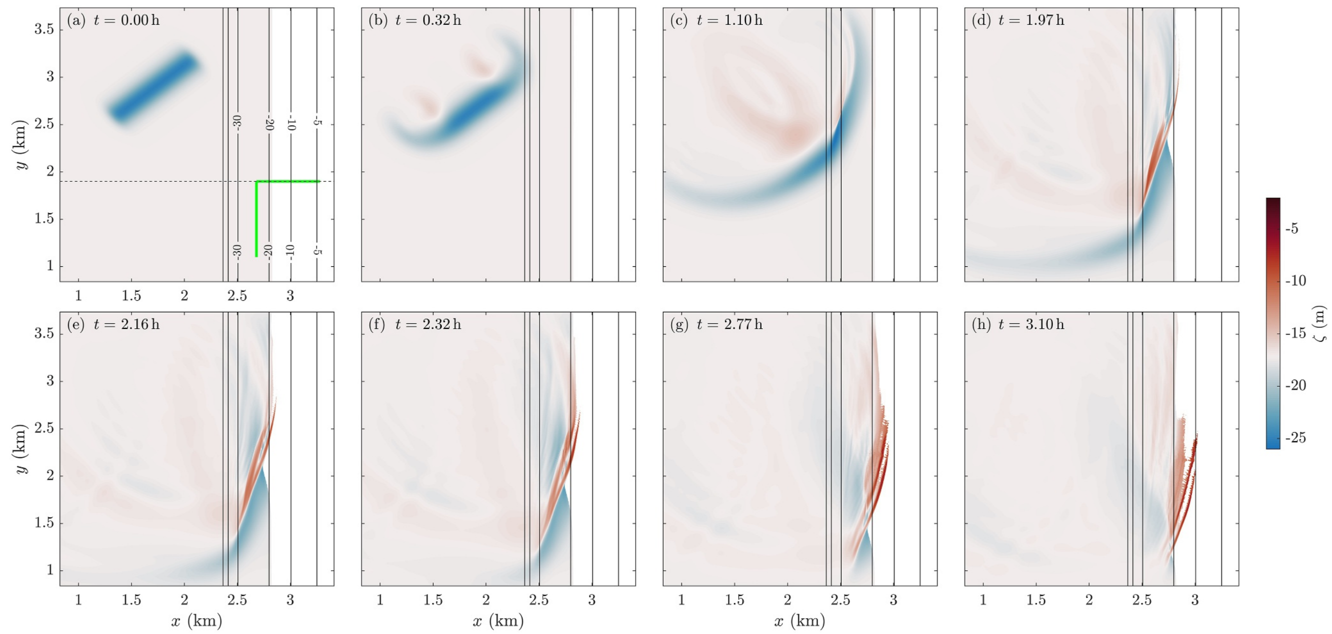

Figure 8. Snapshots of the isosurface $\zeta(x, y, t)$ corresponding to the temperature $T = 14.5$°C. Vertical lines correspond to isobaths plotted every 10 m unless otherwise specified. The white region is the visible part of the seafloor not covered by the isosurface. Panels (a)–(h) correspond to $t = 0$, 0.32, 1.10, 1.97, 2.16, 2.32, 2.77, and 3.10 hr, respectively. In panel (a), the horizontal dashed line corresponds to $y = 1.9$ km for the vertical transect plotted in Figure 9. The green lines represent the L-shaped configuration used to extract the bottom temperature signal shown in Figure 11. Its corner is located at (2.68,1.9) km and the segments extend for 600 and 800 m in the cross-shore and alongshore directions, respectively. As the wave approaches the coastline, it refracts (b–d) and transforms into a wave of elevation, fissioning into multiple crests (e–h).

3.2. Simulated Wave Shoaling Kinematics

3.2.1. Evolution of an Isothermal Surface

First, we examine in Figure 8 the evolution of an isothermal surface η (corresponding to $T = 14.5$°C), selected as a representative proxy within the pycnocline, as the depression wave propagates and shoals. In the early stages of the simulation (panels (a) to (b)), the wave propagates over a flat bottom. Because the initial condition is not an exact solution to the steady-state inviscid problem, the wave undergoes a period of adjustment. This adjustment manifests in the formation of circular patterns at the ends of the truncated nonlinear wave, while the central portion of the wave continues to propagate in the specified direction, albeit with a slightly decreasing amplitude. Similar adjustment patterns are observed in Yuan and Wang (2022); Santilli and Scotti (2015). As time progresses, the northern portion of the wave begins to interact with the seafloor (panel (c)). This part of the wave encounters shallower water, causing it to decelerate relative to the lower portion, which is still advancing in deeper water. Consequently, the wave undergoes a refraction process, leading to a small change in the propagation direction. In panel (c), we observe a steepening of the rear wavefront for 2.25 km $< y <$ 2.75 km. In panel (d), we see the formation of a wave of elevation appearing in red. Its front is mostly straight in the center and appears at an angle with respect to the parallel isobaths. As this wave continues its oblique approach toward the shallower region, we observe the emergence of two distinct long-crested waves of elevation in the top part of the isosurface $y >$ 2 km in panel (e). The crests of the generated elevation waves are, for the most part, nearly parallel. In panels (f) and (g), the crests of the two elevation waves are separated and oriented at an angle to the isobaths as they propagate up the slope, while maintaining a nearly parallel configuration. At the final snapshot (h), the two elevation waves have maintained their coherence as they continue propagating up the slope. Their crests stay well-defined, maintaining both their nearly parallel structure and oblique orientation relative to the isobaths.

To verify that our results are not sensitive to the initial adjustment introduced by truncating the solitary-wave initial condition, we repeated the numerical experiment with the same resolution and an initial wave whose along-crest extent was increased by 50% ($L \approx$ 1.5 km). The associated circular adjustment patterns remain well behind the leading front in the beginning of shoaling, and the resulting dynamics are unchanged, indicating that truncation-related transients do not influence the modeled phenomenon.

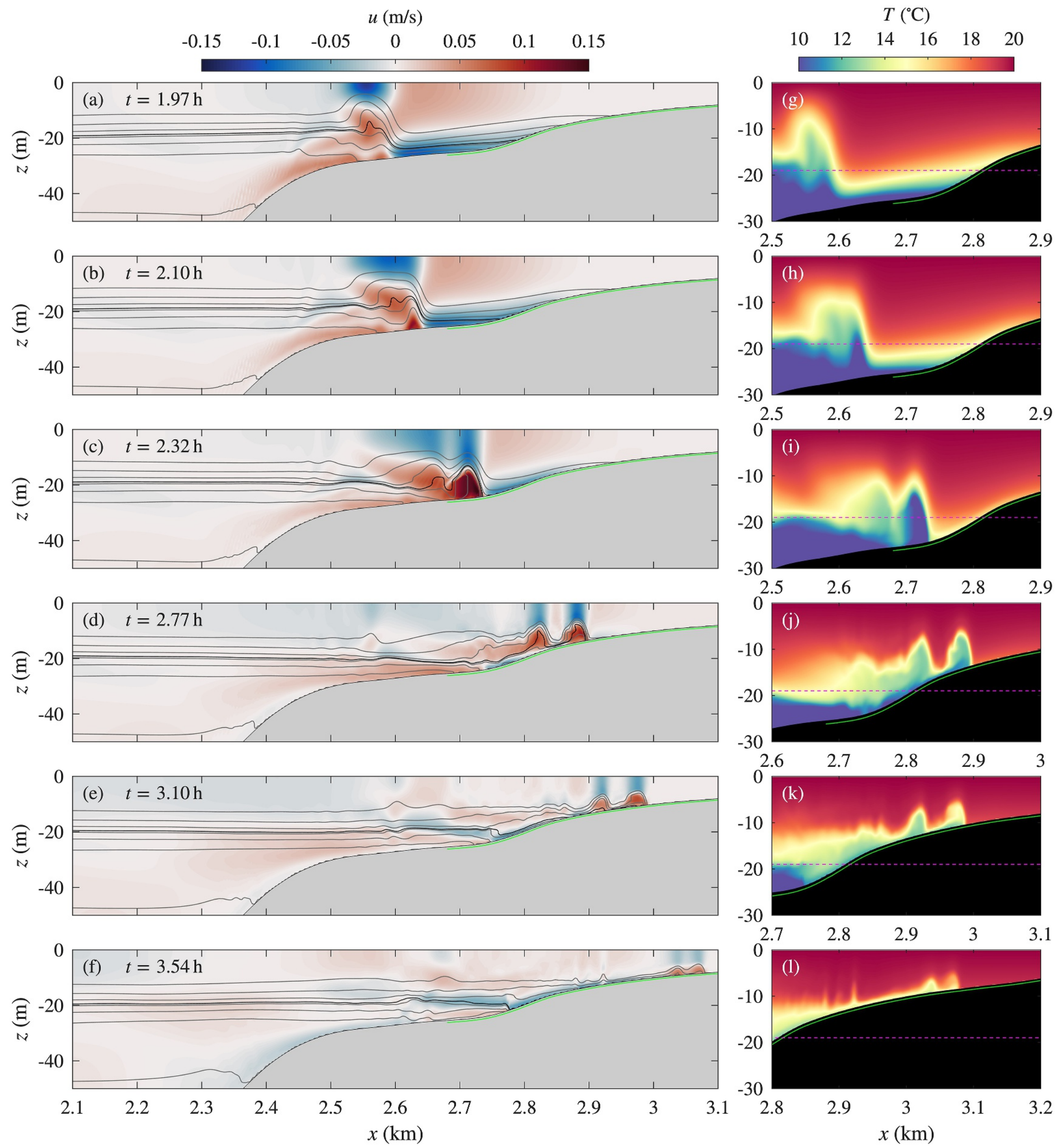

Figure 9. (a)–(f) Snapshots of the horizontal velocity field $u(x, y, z, t)$ evaluated at $y = 1.9$ km, see panel (a) of Figure 8. Isotherms are shown in gray and correspond to [6:2:20]°C. The thermocline corresponding to 12.6°C is shown in black. (g)–(l) Close-up views of the corresponding temperature field. The horizontal dashed magenta line corresponds to the level of the unperturbed thermocline. The green line on the seafloor represents the cross-shore cable used to extract the temperature signature.

3.2.2. Flow Fields

In Figure 9, we consider the evolution of the horizontal velocity field u and temperature T in the vertical cross-section for $y = 1.9$ km (see Figure 8(a)) and for $t \geq 1.97$ h, providing a view of the internal wave dynamics within the water column during shoaling. In panel (a), we see the initial stage of the emergent elevation wave. Below the elevation wave, at around $x = 2.6$ km, we see a small pocket of positive u attached to the bottom, indicating a strong onshore flow adverse to the down-slope local flow for $x > 2.6$ km. Similar structures have been reported in laboratory-scale Direct Numerical Simulations (DNS) (Diamessis & Redekopp, 2006; Hartharn-Evans et al., 2022; Xu & Stastna, 2020) and referred to as separation bubbles. As shown in panels (b) and (c), this region of positive u intensifies and grows in amplitude and magnitude, in accordance to the findings in Xu and Stastna (2020); Hartharn-Evans et al. (2022, 2023). As time progresses, a distinct pulse forms in the flow (panel (c)). As shown in the panels (g)–(i), this pulse has entrapped cold water and extends vertically from several meters below the unperturbed thermocline to several meters above. In the subsequent snapshot (panel (d)), the pulse breaks into two smaller-height pulses, indicating a fission process. Additionally, a near-bottom down-slope flow is observed trailing both the first and second pulses. This flow, also reported in the 2D DNS fission simulations of Aghsaee et al. (2010), indicates that fluid from the pulse interior escapes from the rear of the pulses. In panel (e), as the two pulses propagate up the slope, they lose amplitude, they decelerate and begin to warm, approaching the temperature of the surrounding fluid, see panels (j) and (k). By the final snapshot, the two pulses have nearly merged and lost coherence, until only weak temperature perturbations remain. To complement the above-discussed snapshots, the full dynamical process is illustrated in Movie S1. To verify that the pulse formation is not produced by the truncated initial condition, we carried out a control simulation forced by a shore-normal incident DJL wave with the same stratification, amplitude, and effective Iribarren number as in the reference case. The pulse formation was similar to the oblique case (not shown), confirming that the behavior does not arise from the model setup. We therefore interpret the pulse formation in our case as a genuine fission-like process associated with the wave–slope interaction, consistent with previous numerical studies showing that internal-wave pulses emerge from normally incident waves on gentle slopes (Hartharn-Evans et al., 2023).

3.2.3. Bottom Temperature and Velocity Fields

In Figure 10, we consider the final stages of the evolution of the near-bottom bottom temperature T_{bot} and cross-shore and along-shore near-bottom velocities u_{bot} and v_{bot}. We show the snapshots corresponding to the panels (c)–(f) of Figure 9. The bottom temperature field clearly reveals the signature of an elongated structure transferring cold water upslope, which remains at an oblique angle to the isobaths. This obliqueness is indicative of the combined effects of cross-shore and along-shore motions. The bottom velocity field u_{bot} shows a marked increase in onshore flow (positive u_{bot}), especially concentrated along the advancing structure, indicating the expected increased onshore transport. On the other hand, v_{bot} reveals a significant southward along-shore velocity (negative v_{bot}), which also aligns with the oblique orientation of the structure. It should also be noted that as the elevation wave advances, the elongated patch of positive u_{bot} moves against a negative flow, progressively weakening in velocity amplitude, while the amplitude of negative v_{bot} increases. This pattern indicates a coupling between alongshore and cross-shore flow, shaping the overall bottom signature of this dynamic process. An animation illustrating the evolution of the near-bottom temperature and velocity fields is provided in Movie S2.

3.2.4. Synthetic DTS Signal From Model Output

The numerical solution can be sampled in a manner analogous to the manner in which a seabed fiber optic system samples the coastal ocean. Figure 11a presents a space-time plot of the seafloor temperature extracted from the simulation along two perpendicular segments corresponding to the relative position and orientation of the alongshore and cross-shore cables, and should be compared to Figures 1, and Figures 5 and 6 in Lucas and Pinkel (2022).

The simulation reproduces the main features observed with the temperature-sensing seabed array. The first elevation wave (cf. Figure 8c) appears as a cold track traveling onshore in Figure 11a. Near the intersection of the cables, we find an onshore propagation velocity $v_{p,c} = 0.12$ m/s. This velocity reduces to $v_{p,c} = 0.08$ m/s at a distance ranging from 115 to 254 m from the intersection. In Figure 11b, we examine the evolution of seafloor temperature at the core of the first bolus. During the interval $2.25,\mathrm{h} \leq t \leq 3.2,\mathrm{h}$, when the bolus is well developed, the core warms at a rate of approximately $0.003\,^{\circ}\mathrm{C/s}$, in agreement with the mean warming rate reported by Lucas and Pinkel (2022) based on multiple shoaling events. As discussed in that study, this rate is too large to be explained by typical values of vertical diffusivity in the ocean and is instead attributed to the entrainment of warm ambient water into the cold bolus core. The simulation suggests that the source of this entrainment is primary via the back-face of the bolus (Figure 9(c)). A full analysis of the entrainment process is left for a future investigation. For context, Lucas and Pinkel (2022) inferred from DTS observations internal boluses of amplitude of ~ 5 m over 12–15 m depths, underscoring a strongly nonlinear regime that is also represented in our simulations.

The imprint of the fission process can be seen in the trajectories of two cold pulses that eventually collide at about $t = 4$ h. This occurs because the dissipating leading wave slows and is overtaken by the larger following wave. This "inverted-Y" signature is present in the observed data (cf. Figure 3a).

10.1029/2025JC022650

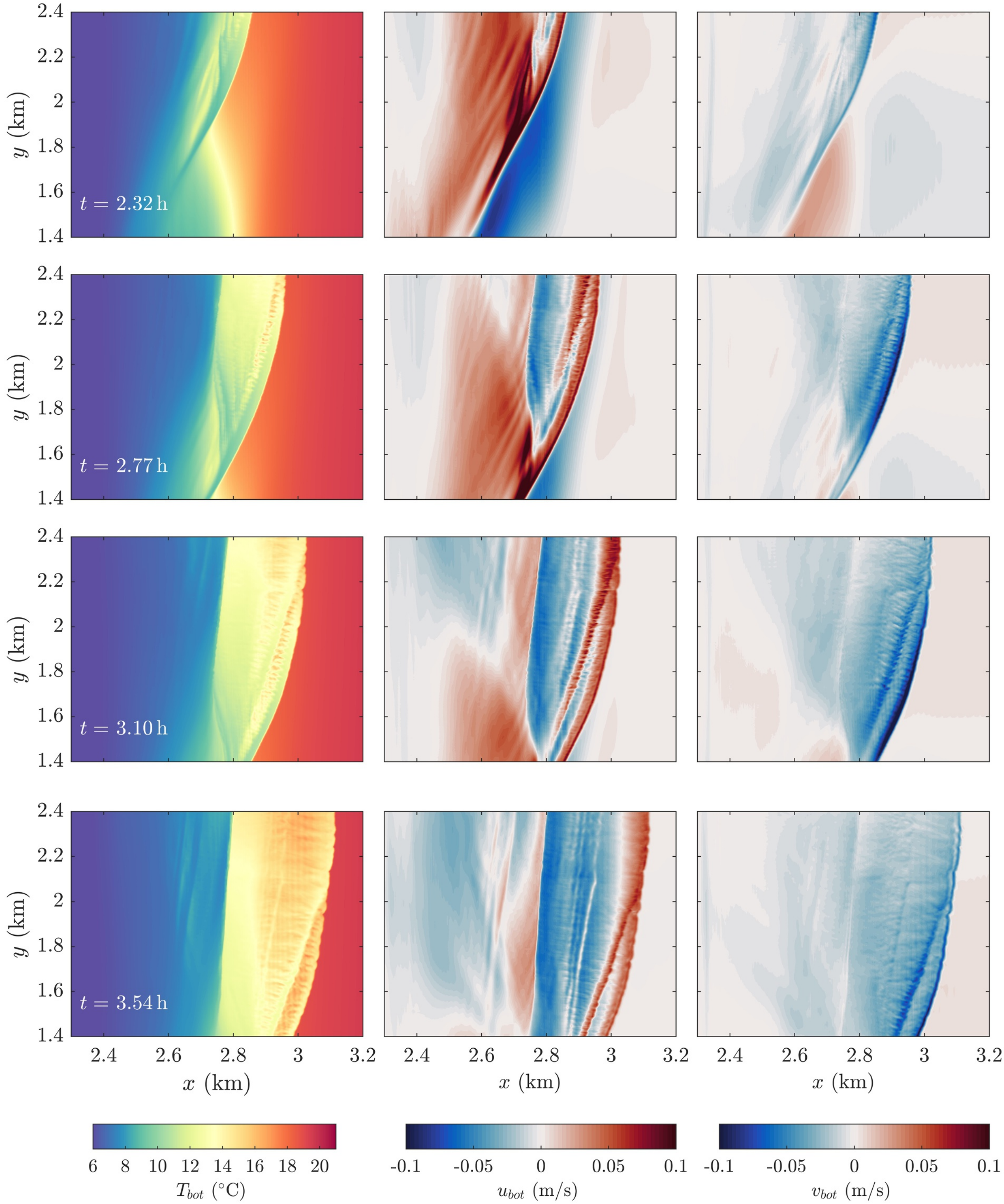

Figure 10. Snapshots of the near-bottom temperature T_{bot}, and horizontal velocity fields u_{bot} and v_{bot} at $t = 2.32$, 2.77, 3.10 and 3.54 hr.

The values extracted from the simulation align well with the dominant values obtained from the analysis in Section 2. This agreement suggests that the signatures captured by the DTS fibers are consistent with boluses of cold water generated by the fission of obliquely shoaling depression waves.

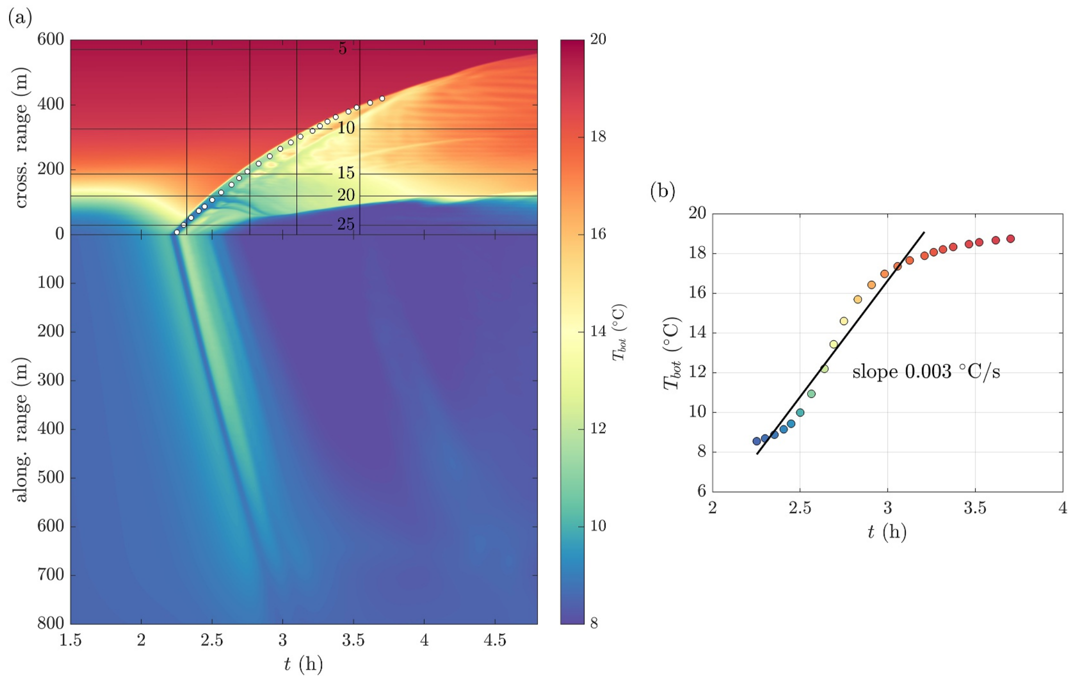

Figure 11. (a) Space-time plot of the simulated near-bottom temperature T_{bot} corresponding to the segments shown in panel (a) of Figure 8. Horizontal lines indicate isobaths, while vertical black lines mark $t = 2.32$, 2.77, 3.20, and 3.54 hr (see Figures 9c–9f). White bullets trace the trajectory of the bolus. (b) Bolus seafloor temperature as a function of time. The straight black line represents a linear fit to the simulation data over the interval 2.25 h $\leq t \leq$ 3.2 h when the bolus is well developed.

3.2.5. Small-Scale Along-Crest Variability Near the Seabed

Here, we focus on the small-scale transverse oscillations that appear at the trailing edge of the simulated seabed signature of the boluses (Figure 10). In particular, we examine the hypothesis proposed by Lucas and Pinkel (2022), who suggested that the small-scale variability observed in the cross-shore cable signature arises from alongshore structures advected perpendicular to the cross-shore cable. In their study, Lucas and Pinkel (2022) estimated the vertical displacement field on the bottom based on this hypothesis and the seafloor temperature data. Here, we directly calculate it from our simulation data.

The vertical displacement $\eta(x, y, z, t)$ represents the vertical shift of a fluid parcel from its reference position in the background density field and is defined as $\eta = z - z_*$, where $z_*(x, y, z, t)$ denotes the reference position that the fluid parcel would occupy in the unperturbed background state (Kang & Fringer, 2010). To estimate z_*, we use the stable background density profile, say $\rho_0(z)$, and the perturbed density field $\rho(x, y, z, t)$ resulting from the simulation. The density of the fluid parcel satisfies the relation $\rho(x, y, z, t) = \rho_0(x, y, z_*, t)$ which can be inverted at any (x, y, t) to find z_* and consequently η. If density overturns are present at some (x, y, t), the density field ρ requires sorting into a vertically stable configuration prior to inversion.

A snapshot of the near-bottom vertical displacement, η_{bot}, at $t = 3.10$ h, and the horizontal near-bottom velocity field $(u_{\text{bot}}, v_{\text{bot}})$ is shown in Figure 12. The data are presented in a rotated reference frame, $Ox'y'$, with its origin located within the first bolus at (2.973, 1.862) m (see Figure 10). The frame is rotated 10° clockwise such that the y' axis is approximately aligned with the crest of the bolus. The simulated η_{bot} is in very good agreement with the observational reconstruction of Lucas and Pinkel (2022), Figure 9). In particular, we observe an abrupt frontal structure at the leading edge of the boluses. Pronounced transverse undulations emerge from their trailing edge, with elevations initially comparable to those of the boluses and decreasing with distance. The associated horizontal velocities are predominantly directed southward, with occasional offshore components. These results support the interpretation that the observed high-frequency transverse oscillations in bottom temperature arise from quasi-alongshore structures advected southward by the flow, consistent with the hypothesis of Lucas and Pinkel (2022).

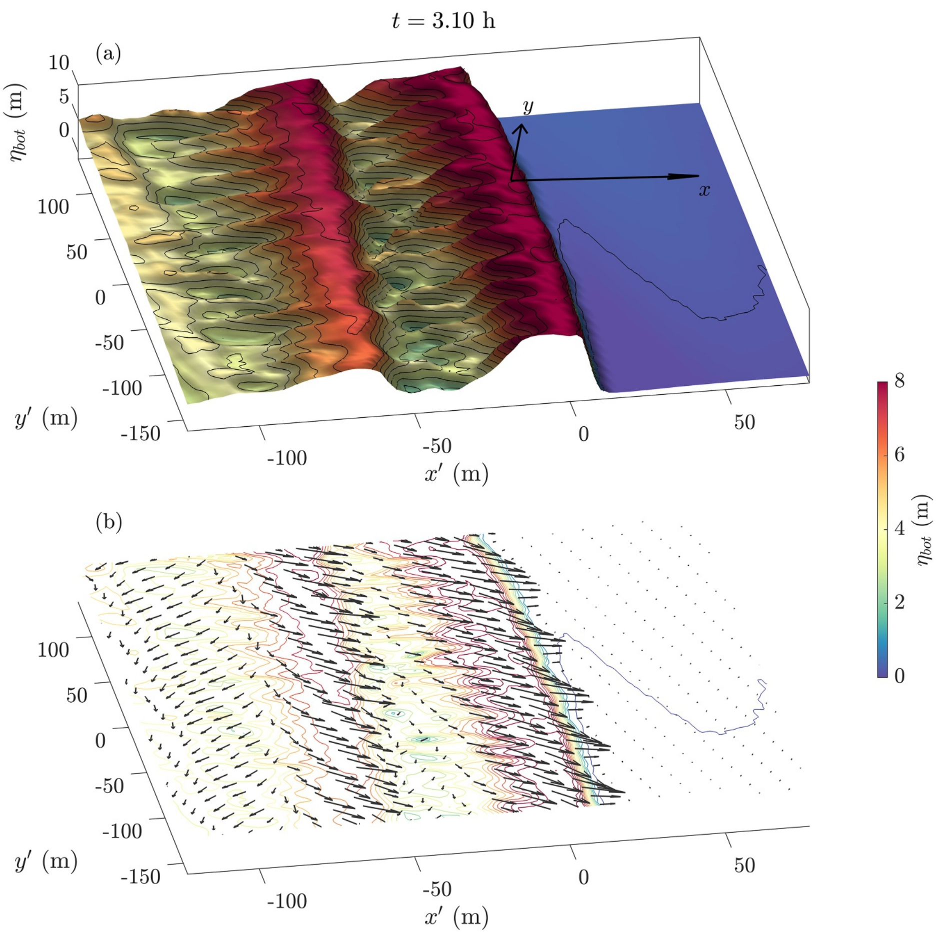

Figure 12. (a) Near-bottom vertical displacement field η_{bot} at $t = 3.10$ h. (b) Near-bottom horizontal velocity field $(u_{\text{bot}}, v_{\text{bot}})$ in a rotated frame of reference $(Ox'y')$ superimposed with the iso-contours of η. Both the velocity field and the iso-contours are projected onto a reference horizontal plane for visualization.

3.2.6. Flow and Vortical Structures Within the Fluid Domain

Having identified small-scale along-crest undulations near the seabed trailing the boluses in the model, consistent with observations, it is natural to also present the vertical structure of the flow. Figure 13 presents the same snapshot as in Figure 12, focusing on flow quantities evaluated on vertical planes within the region encompassing the boluses, $x \in [2850, 3000]$ m, $y \in [1700, 1950]$ m. The internal wave form is visualized using the isothermal surface of $T = 14.5$°C, shown in transparent yellow.

We first examine the y-component of velocity, v, presented in the top row. In the vertical plane at $y = 1950$ m, which intersects the crests of the boluses we observe a region of strong negative v (directed toward decreasing y) following approximately the shape of the isothermal curve (black dashed line). Above this curve, v changes sign abruptly and is larger above the crests of the boluses. To examine the along-crest flow we consider vertical planes approximately aligned with the crests of the boluses. We introduce two rotated reference frames, $(\tilde{x}_1, \tilde{y}_1)$ and $(\tilde{x}_2, \tilde{y}_2)$, such that $\tilde{y}_1$ and $\tilde{y}_2$ are aligned with the crests of the first and second bolus, respectively, and $\tilde{x}_1$, $\tilde{x}_2$ represent the instantaneous propagation direction. The angles of rotation are $\phi_1 = 10°$ and $\phi_2 = 13°$, respectively. These planes are then translated along $\tilde{x}_1$ and $\tilde{x}_2$ to capture the along-crest flow at the front, interior, and rear of each bolus. For brevity, we omit the subscripts on $(\tilde{x}, \tilde{y})$ when possible and the distinction between the two frames is unambiguous.

Panels (a)–(c) show the horizontal velocity field (u, v) projected onto the along-crest directions, denoted by $\tilde{v}$. A strong southward along-crest flow (toward decreasing $\tilde{y}$) is established within the boluses, with an abrupt reversal at higher vertical elevations. This pronounced, large-scale along-crest flow arises from the oblique incidence

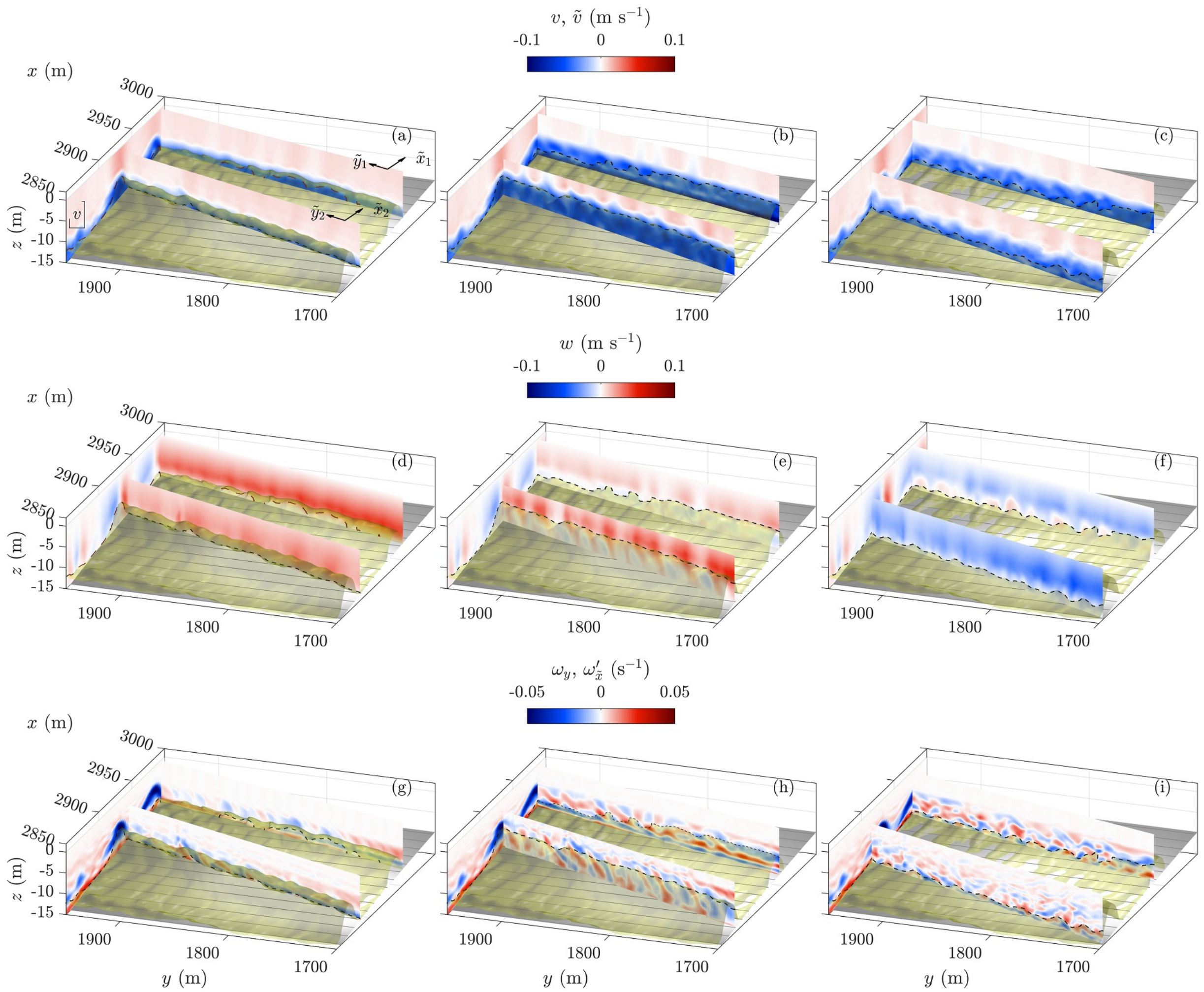

Figure 13. Velocity fields and vorticity in the presence of boluses at $t = 3.10$ h. The yellow transparent surface represents the isothermal contour at $T = 14.5$°C. The (x, z)-plane on the left of each panel corresponds to the section at $y = 1950$ m. The two interior planes in each panel are rotated to align with the nearly straight crests of the boluses, with their corresponding reference frames denoted by $(\tilde{x}_1, \tilde{y}_1)$ and $(\tilde{x}_2, \tilde{y}_2)$. From left to right, the planes are positioned at the front, at the interior, and at the rear of the boluses. Panels (a)–(c) display the spanwise velocity component v at $y = 1950$ m. The interior planes show the along-crest projections of the horizontal velocity field (u, v), denoted by $\tilde{v}$. Panels (d)–(f) show the vertical velocity w at the same locations. Panels (g)–(i) present the y-component of vorticity ω_y at $y = 1950$ m and the perturbation vorticity $\omega'_{\tilde{x}}$ on the along-crest planes. Dashed curves represent the intersection of the isothermal with the vertical planes.

configuration considered in the present setup. Smaller-scale perturbations in $\tilde{v}$ along the crest are also evident in all three locations reflecting the fine three-dimensional structure of the flow. The emergence of such flows suggests the presence of wave-induced transport along the crest, driven by the oblique propagation and three-dimensional deformation of the boluses. The simulated horizontal velocities indicate along-crest and vertical gradients that can influence how momentum is redistributed as the waves shoal. In the shoaling bolus, the flow organizes into a narrow, vertically sheared along-crest current. Because this flow is also confined, cross-shore variations in its strength create localized shear regions. Three-dimensional perturbations amplify within these regions, producing along-crest undulations.

In panels (d)–(f), we plot the vertical velocity w. On the plane $\{y = 1950\}$ m, w has the expected trend associated to an internal wave of elevation propagating toward increasing x; Ahead of the bolus crest, the fluid experiences upward motion, while behind the bolus, a downward motion. Outside the front and rear of the wave, the vertical velocity rapidly decays to zero, consistent with the solitary nature of the boluses. In the along-crest direction there is significant variability in w, especially in the interior and near the rear face of the boluses.

Finally, panels (g)–(i) present sections of the vorticity field associated with the flow. On the $y = 1950$ m plane, we show the y-component of vorticity, $\omega_y = \partial_z u - \partial_x w$. The boluses exhibit a significant counterclockwise vortex structure (negative ω_y), accompanied by significant near-bottom clockwise ω_y. Next, we are interested on the component of vorticity normal to the along-crest planes, defined as $\omega_{\tilde{x}} = \partial_{\tilde{y}} w - \partial_z \tilde{v}$, in order to identify vortical structures that are approximately aligned with the direction of wave propagation. The top two rows of the figure indicate that the velocity field $(\tilde{v}, \tilde{w})$, evaluated on the along-crest $(\tilde{y}, z)$ planes, can be decomposed into a background component and a perturbation:

$$\tilde{v}' = \tilde{v} - \langle \tilde{v} \rangle_{\tilde{y}}, \quad \tilde{w}' = \tilde{w} - \langle \tilde{w} \rangle_{\tilde{y}}, \tag{4}$$

where $\langle \cdot \rangle_{\tilde{y}}(z)$ denotes the spatial average along the $\tilde{y}$-direction within each plane. Based on this decomposition, we compute the perturbation vorticity field $\omega'_{\tilde{x}} = \partial_{\tilde{y}} \tilde{w}' - \partial_z \tilde{v}'$, shown in the bottom row of the figure. This quantity isolates the small-scale, three-dimensional vortical structures superimposed on the background flow. Regions of intensified perturbation vorticity are mainly concentrated near the bottom boundary, particularly within the interior and at the rear of the boluses. These along-crest perturbations suggest the presence of localized shear instabilities linked to the dynamics of the boluses. The trailing vortices and along-crest undulations point to the three-dimensional secondary instability pathway described for lobe-and-cleft formation in density-current fronts (Shi et al., 2024). The fact that these vortices are concentrated near the seabed suggests the development of near-bottom mixing, which may play a important role in energy dissipation and momentum transfer within the shoaling zone. A useful metric for instability onset would be to calculate a 2D/3D kinetic-energy partition along the evolution, as was done recently in the normal-incidence case Castro-Folker and Stastna (2024). However, applying this approach here would require an orientation-tracked, crest-aligned decomposition to handle obliquely incident, time-evolving, curved crests. This is beyond our present scope but a promising direction for future work.

3.3. Sensitivity

We close this section by presenting results from a sensitivity analysis conducted to examine the impact of key simulation parameters. Figure 14 illustrates the simulated cross-shore bottom signature, dT_{bot}/dt, for 9 different simulations labeled as Run 1–9 in Table 1.

These trials show that this process is largely unaffected by small variations in background stratification or incident wave amplitude. Instead, it appears that the mild-slope topographic conditions of the studied region promote the fission of incident depression solitary-like internal waves into bottom-attached pulses. The modeled wave transformation closely resembles the observed wave structures, as shown in Figures 3 and 14, highlighting the ability of the idealized model in capturing key dynamical features. While the model closely reproduces the dominant observed traveling speed of these pulses when $N_{\max} = 0.0019$ 1/s, it predicts trajectories that persist longer than what is observed in nature.

Here, it is worth noting that in the runs corresponding to weaker stratification (Run 2) and smaller initial amplitude (Run 6) relative to the reference case, a bolus still forms, while the trailing undulations are noticeably less pronounced. A systematic assessment of how stratification and wave amplitude control the onset and strength of the observed instabilities would require a dedicated parameter sweep and vorticity-based diagnostics, and is a natural next step that will be pursued in future work.

4. Conclusions

We identified internal-wave shoaling events from fiber optic seafloor temperature measurements utilizing a time-domain approach that relies on the cross-correlation of the observed signal with prototypical signals corresponding to different propagation velocities. The majority of shoaling nonlinear internal waves arrived preferentially near the minimum ebb phase of the internal tide, when the thermocline was the deepest. This suggests that the incident wave and stratification conditions during the 'ebb-tide' favor bottom-attached bolus formation by enabling an earlier and stronger interaction between the incident wave trough and the slope, promoting boundary-layer separation and suppressing a more gradual disintegration of the incident wave into free non-bottom-attached elevation waves. The precise mechanism by which tidal phase modulates the incident nonlinear waves and their shoaling details, however, remains an open question and requires a dedicated tide-resolved study. The shoaling

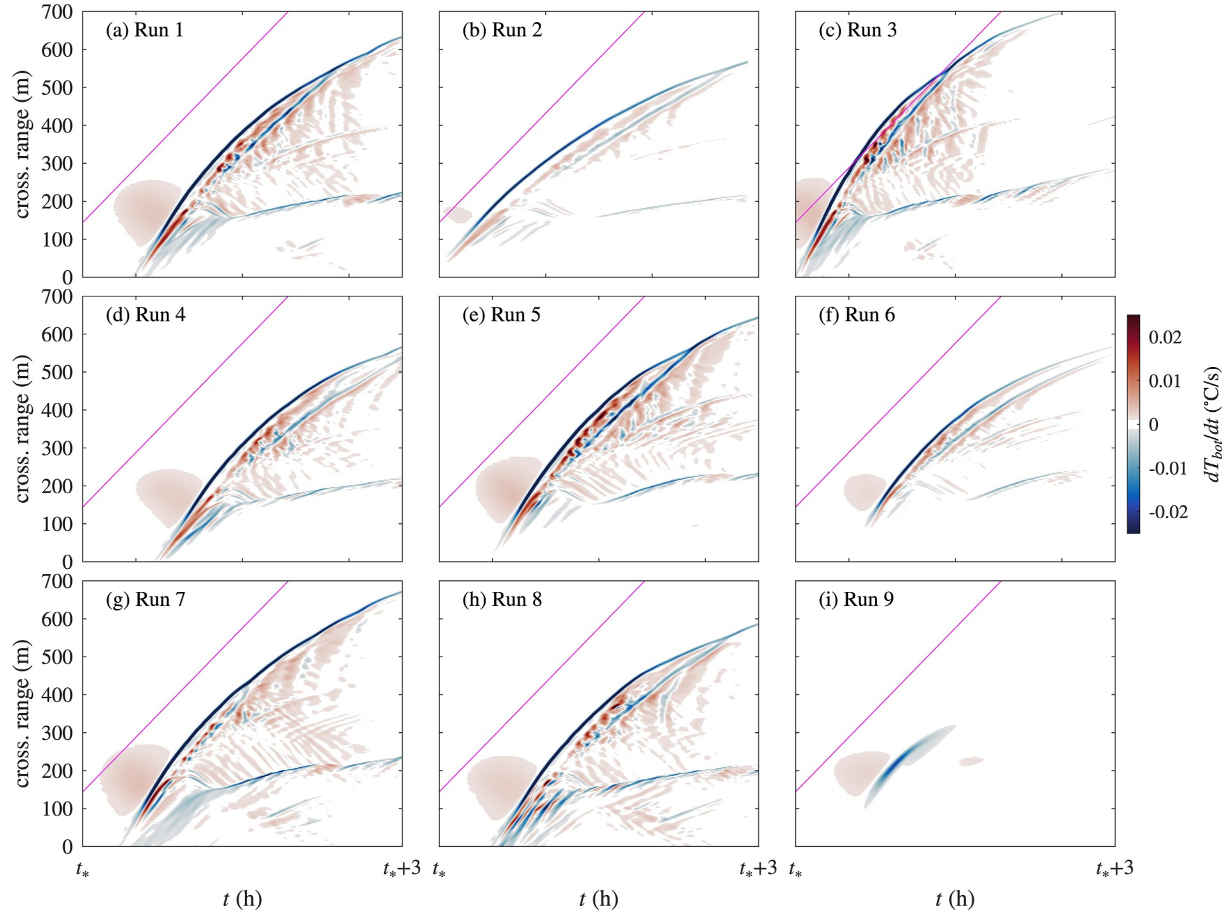

Figure 14. Space-time plots of the rate of change of the seafloor temperature signature (dT_{bot}/dt) evaluated along the cross-shore cable for the cases listed in Table 1. The magenta line corresponds to a constant propagation velocity of 0.08 m/s.

Table 1
Summary of the Different Parameters Used in the Sensitivity Runs. N_{max}, L_N and H_N are the Parameters in the Stratification (See Equation 2). A and c_{DJL} are the Amplitude and Phase Speed of the Initial Solitary-Like Wave of Depression Computed Using the DJL Equation In Run 9, We Repeat Run 1 With Different Viscosity and Diffusivity Coefficients (Shown in $m^2\ s^{-1}$)

	$N_{\max}$ (s^{-1})	L_N (m)	H_N (m)	A (m)	c_{DJL} (m/s)
Run 1	0.019	20	19	8	0.25
Run 2	0.013	20	19	8	0.17
Run 3	0.025	20	19	8	0.32
Run 4	0.019	15	19	8	0.22
Run 5	0.019	20	17	8	0.26
Run 6	0.019	20	19	5	0.24
Run 7	0.019	25	19	8	0.26
Run 8	0.019	20	21	8	0.25
Run 9	Run 1 with $\nu_b = 10^{-3}$, $\kappa_b = 10^{-5}$ $\nu_0 = 1.5 \times 10^{-2}$, $\nu_h = \kappa_h = 0.1$				

waves had propagation speeds of ∼10 cm/s, periods of ∼10 min, and approached the coast from a direction of ∼20° clockwise of shore-normal. Our approach systematically characterizes shoaling patterns that are not easily identified by standard spectral methods, highlighting the value of a space-time approach in studying intermittent and spatially localized wave dynamics from the high-bandwidth measurements produced by distributed fiber optic sensing techniques. In its present form, the method uses straight, constant-speed prototypes. This idealized library is sufficient to identify the dominant, well-developed shoaling events and to quantify their occurrence and speeds. Exapanding it to include more complex propagation patterns (curved, accelerating/decelerating trajectories) would enable the method to capture a broader range of wave behaviors.

We used the wave observations as the inspiration for 3D non-hydrostatic MITgcm simulations using an idealized configuration of oblique wave shoaling and the PP81 parametrization scheme to model unresolved processes. The goal was to reproduce key features of the seafloor temperature signatures measured by the fiber optic seabed array and to deepen our understanding of the underlying shoaling dynamics. In the model, an initial solitary-like depression wave shoals obliquely over an alongshore-uniform shoaling bathymetry representing the transect where the cross-shore cable was deployed. By analyzing the simulated wave fields, we demonstrated that during the interaction between the incident depression wave and the seafloor, a bottom-attached structure forms, trapping cold water and subsequently moving up the slope. This bottom-attached structure closely resembles the separation bubble observed in high-resolution laboratory-scale DNS simulations. In fact, when examining the horizontal velocity field, there is a striking qualitative agreement between the present large-scale simulations (Figure 9), the experimental observations of Ghassemi et al. (2022) (their Figure 13), and the DNS results in Hartharn-Evans et al. (2023) (their Figure 2). In our 3D simulations, fission emerges from the oblique interaction of a solitary-like depression wave with a mildly sloping bathymetry, producing two long-crested, bottom-attached elevation pulses that propagate upslope at an angle to the isobaths. The reconstructed seafloor-temperature signal from the simulation shows good qualitative agreement with the DTS observations and the onshore propagation velocities and timing differences of the pulse trajectories align closely with those inferred from the data. The simulations also uncover a strong alongshore near-bottom flow, pointing to an alongshore transport, even though this is not quantified here. To our knowledge, these are the first 3D parametrized simulations to reproduce the seafloor signature of shoaling-induced fission at realistic scales. We have also shown that the process is robust to small variations in background stratification. Furthermore, it occurs under oblique incidence building on prior laboratory and DNS studies that demonstrated this process under normal incidence. This finding is especially relevant to the study region, where internal waves approach the slope at an angle due to the local generation at the nearby Scripps Branch of the La Jolla Canyon.

The primary limitation of the present model is the assumption of a single isolated incident solitary wave-like form, whereas observations suggest that multiple incident waves contribute to the complex wave dynamics in the region of interest. Furthermore, the bathymetry is also simplified, as we assumed no variability in the transverse direction, thereby neglecting potential transverse large-scale perturbations that may influence energy redistribution. Despite these simplifications, the model still achieves good qualitative agreement with observations. Since simulations at this scale rely on parametrization of sub-grid processes, additional observational data, including velocity measurements throughout the water column and near-bed Reynold's stress estimation, are required for further progress. These factors are essential for refining the model's predictive capabilities and will be the focus of future investigations.

Conflict of Interest

The authors declare no conflicts of interest relevant to this study.

Availability Statement

The Massachusetts Institute of Technology general circulation model used for the simulations is available at https://mitgcm.org/source-code/. The solver of the DJL equation is available at https://github.com/mdunphy/DJLES. Data and software used to produce the figures are publicly available at Papoutsellis et al. (2026).

Acknowledgments
This work was supported by ONR Grants N00014-22-1-2730 and N00014-23-1-2233 to A.J. Lucas and O. Schmidt.

References

Aghsaee, P., Boegman, L., & Lamb, K. (2010). Breaking of shoaling internal solitary waves. *Journal of Fluid Mechanics*, *659*, 289–317. https://doi.org/10.1017/s002211201000248x

Arthur, R. S., & Fringer, O. B. (2016). Transport by breaking internal gravity waves on slopes. *Journal of Fluid Mechanics*, *789*, 93–126. https://doi.org/10.1017/jfm.2015.723

Bai, X., Liu, Z., Zheng, Q., Hu, J., Lamb, K. G., & Cai, S. (2019). Fission of shoaling internal waves on the northeastern shelf of the South China Sea. *Journal of Geophysical Research: Oceans*, *124*(7), 4529–4545. https://doi.org/10.1029/2018jc014437

Boegman, L., & Stastna, M. (2019). Sediment resuspension and transport by internal solitary waves. *Annual Review of Fluid Mechanics*, *51*(1), 129–154. https://doi.org/10.1146/annurev-fluid-122316-045049

Bowers, J., Morton, I., & Mould, G. (2000). Directional statistics of the wind and waves. *Applied Ocean Research*, *22*(1), 13–30. https://doi.org/10.1016/S0141-1187(99)00025-5

Castro-Folker, N., & Stastna, M. (2024). On the three-dimensional structure of instabilities beneath shallow-shoaling internal waves. *Journal of Fluid Mechanics*, *995*, R2. https://doi.org/10.1017/jfm.2024.703

Cheriton, O. M., McPhee-Shaw, E. E., Shaw, W. J., Stanton, T. P., Bellingham, J. G., & Storlazzi, C. D. (2014). Suspended particulate layers and internal waves over the southern Monterey Bay Continental shelf: An important control on shelf mud belts? *Journal of Geophysical Research: Oceans*, *119*(1), 428–444. https://doi.org/10.1002/2013jc009360

Colosi, J. A., Kumar, N., Suanda, S. H., Freismuth, T. M., & MacMahan, J. H. (2018). Statistics of internal tide bores and internal solitary waves observed on the inner Continental shelf off point Sal, California. *Journal of Physical Oceanography*, *48*(1), 123–143. https://doi.org/10.1175/JPO-D-17-0045.1

Dauhajre, D. P., Molemaker, M. J., McWilliams, J. C., & Hypolite, D. (2021). Effects of stratification on shoaling internal tidal bores. *Journal of Physical Oceanography*, *51*(10), 3183–3202. https://doi.org/10.1175/jpo-d-21-0107.1

Dauxois, T., Didier, A., & Falcon, E. (2004). Observation of near-critical reflection of internal waves in a stably stratified fluid. *Physics of Fluids*, *16*(6), 1936–1941. https://doi.org/10.1063/1.1711814

Davis, K. A., Arthur, R. S., Reid, E. C., Rogers, J. S., Fringer, O. B., DeCarlo, T. M., & Cohen, A. L. (2020). Fate of internal waves on a shallow shelf. *Journal of Geophysical Research: Oceans*, *125*(5), e2019JC015377. https://doi.org/10.1029/2019jc015377

Davis, K. A., Leichter, J. J., Hench, J. L., & Monismith, S. G. (2008). Effects of Western boundary current dynamics on the internal wave field of the southeast Florida shelf. *Journal of Geophysical Research*, *113*(C9), C09010. https://doi.org/10.1029/2007JC004699

Davis, K. A., & Monismith, S. G. (2011). The modification of bottom boundary layer turbulence and mixing by internal waves shoaling on a barrier reef. *Journal of Physical Oceanography*, *41*(11), 2223–2241. https://doi.org/10.1175/2011jpo4344.1

Diamessis, P. J., & Redekopp, L. G. (2006). Numerical investigation of solitary internal wave-induced global instability in shallow water benthic boundary layers. *Journal of Physical Oceanography*, *36*(5), 784–812. https://doi.org/10.1175/jpo2900.1

Dunphy, M., Subich, C., & Stastna, M. (2011). Spectral methods for internal waves: Indistinguishable density profiles and double-humped solitary waves. *Nonlinear Processes in Geophysics*, *18*(3), 351–358. https://doi.org/10.5194/npg-18-351-2011

Emery, K. O., & Gunnerson, C. G. (1973). Internal swash and surf. *Proceedings of the National Academy of Sciences*, *70*(8), 2379–2380. https://doi.org/10.1073/pnas.70.8.2379

Fisher, N. I. (1995). *Statistical analysis of circular data*. Cambridge University Press.

Garrett, C., & Munk, W. (1979). Internal waves in the ocean. *Annual Review of Fluid Mechanics*, *11*(1), 339–369.

Ghassemi, A., Zahedi, S., & Boegman, L. (2022). Bolus formation from fission of nonlinear internal waves over a mild slope. *Journal of Fluid Mechanics*, *932*, A50. https://doi.org/10.1017/jfm.2021.1033

Guo, D., Zhan, P., & Hoteit, I. (2021). Three-dimensional simulation of shoaling internal solitary waves and their influence on particle transport in the Southern Red Sea. *Journal of Geophysical Research: Oceans*, *126*(4), e2020JC016335. https://doi.org/10.1029/2020jc016335

Hartharn-Evans, S. G., Carr, M., Stastna, M., & Davies, P. A. (2022). Stratification effects on shoaling internal solitary waves. *Journal of Fluid Mechanics*, *933*, A19. https://doi.org/10.1017/jfm.2021.1049

Hartharn-Evans, S. G., Stastna, M., & Carr, M. (2023). Dense pulses formed from fissioning internal waves. *Environmental Fluid Mechanics*, *23*(2), 389–405. https://doi.org/10.1007/s10652-022-09894-x

He, X., Chen, X., Li, Q., Xu, T., & Meng, J. (2023). Numerical simulations and an updated parameterization of the breaking internal solitary wave over the Continental shelf. *Journal of Geophysical Research: Oceans*, *128*(11), e2023JC019975. https://doi.org/10.1029/2023jc019975

Helfrich, K. R., & Melville, W. K. (2006). Long nonlinear internal waves. *Annual Review of Fluid Mechanics*, *38*(1), 395–425. https://doi.org/10.1146/annurev.fluid.38.050304.092129

Hosegood, P., Bonnin, J., & van Haren, H. (2004). Solibore-induced sediment resuspension in the faeroe-shetland channel. *Geophysical Research Letters*, *31*(9). https://doi.org/10.1029/2004gl019544

Kalai, C., & Mondal, A. (2022). A non-parametric circular statistics-based framework for predicting peak flow seasonality at ungauged sites. *Water Resources Research*, *58*(8), e2021WR031004. https://doi.org/10.1029/2021WR031004

Kang, D., & Fringer, O. (2010). On the calculation of available potential energy in internal wave fields. *Journal of Physical Oceanography*, *40*(11), 2539–2545. https://doi.org/10.1175/2010JPO4497.1

Klymak, J. M., & Moum, J. N. (2003). Internal solitary waves of elevation advancing on a shoaling shelf. *Geophysical Research Letters*, *30*(20). https://doi.org/10.1029/2003gl017706

Locarnini, R. A., Mishonov, A. V., Baranova, O. K., Reagan, J. R., Boyer, T. P., Seidov, D., et al. (2024). World ocean atlas 2023. *Temperature (Austin)*, Vol. 1. https://doi.org/10.25923/54bh-1613. (A. Mishonov, Technical Editor. NOAA Atlas NESDIS 89)

Lucas, A. J., Franks, P. J., & Dupont, C. L. (2011). Horizontal internal-tide fluxes support elevated phytoplankton productivity over the inner Continental shelf. *Limnology and Oceanography: Fluids and Environments*, *1*(1), 56–74. https://doi.org/10.1215/21573698-1258185

Lucas, A. J., & Pinkel, R. (2022). Observations of coherent transverse wakes in shoaling nonlinear internal waves. *Journal of Physical Oceanography*, *52*(6), 1277–1293. https://doi.org/10.1175/jpo-d-21-0059.1

MacKinnon, J., & Gregg, M. (2003). Mixing on the late-summer new England shelf—Solibores, shear, and stratification. *Journal of Physical Oceanography*, *33*(7), 1476–1492. https://doi.org/10.1175/1520-0485(2003)033<1476:motlne>2.0.co;2

Marshall, J., Adcroft, A., Hill, C., Perelman, L., & Heisey, C. (1997). A finite-volume, incompressible navier stokes model for studies of the ocean on parallel computers. *Journal of Geophysical Research*, *102*(C3), 5753–5766. https://doi.org/10.1029/96jc02775

McSweeney, J. M., Lerczak, J. A., Barth, J. A., Becherer, J., Colosi, J. A., MacKinnon, J. A., et al. (2020). Observations of shoaling nonlinear internal bores across the central California inner shelf. *Journal of Physical Oceanography*, *50*(1), 111–132. https://doi.org/10.1175/jpo-d-19-0125.1

Michallet, H., & Ivey, G. N. (1999). Experiments on mixing due to internal solitary waves breaking on uniform slopes. *Journal of Geophysical Research*, *104*(C6), 13467–13477. https://doi.org/10.1029/1999jc900037

Omand, M. M., Leichter, J. J., Franks, P. J., Guza, R., Lucas, A. J., & Feddersen, F. (2011). Physical and biological processes underlying the sudden surface appearance of a red tide in the nearshore. *Limnology & Oceanography*, *56*(3), 787–801. https://doi.org/10.4319/lo.2011.56.3.0787

Orr, M. H., & Mignerey, P. C. (2003). Nonlinear internal waves in the South China Sea: Observation of the conversion of depression internal waves to elevation internal waves. *Journal of Geophysical Research*, *108*(C3). https://doi.org/10.1029/2001jc001163

Pacanowski, R. C., & Philander, S. G. H. (1981). Parameterization of vertical mixing in numerical models of tropical oceans. *Journal of Physical Oceanography*, *11*(11), 1443–1451. https://doi.org/10.1175/1520-0485(1981)011<1443:povmin>2.0.co;2

Papoutsellis, C. E., Lucas, A. J., Shukla, I., Okun, K. M., Pinkel, R., & Schmidt, O. T. (2026). Obliquely incident nonlinear internal waves on a shallow shelf [Supporting data and software]. *Zenodo*. https://doi.org/10.5281/zenodo.19162000

Pineda, J. (1991). Predictable upwelling and the shoreward transport of planktonic larvae by internal tidal bores. *Science*, *253*(5019), 548–549. https://doi.org/10.1126/science.253.5019.548

Santilli, E., & Scotti, A. (2015). The stratified ocean model with adaptive refinement (Somar). *Journal of Computational Physics*, *291*, 60–81. https://doi.org/10.1016/j.jcp.2015.03.008

Shi, F., Simpson, A., & Hsu, T.-J. (2024). Modeling lobe-and-cleft instabilities on a river plume. *Journal of Geophysical Research: Oceans*, *129*(5), e2023JC020485. https://doi.org/10.1029/2023JC020485

Sinnett, G., Davis, K. A., Lucas, A. J., Giddings, S. N., Reid, E., Harvey, M. E., & Stokes, I. (2020). Distributed temperature sensing for oceanographic applications. *Journal of Atmospheric and Oceanic Technology*, *37*(11), 1987–1997. https://doi.org/10.1175/jtech-d-20-0066.1

Sinnett, G., Feddersen, F., Lucas, A. J., Pawlak, G., & Terrill, E. (2018). Observations of nonlinear internal wave run-up to the surfzone. *Journal of Physical Oceanography*, *48*(3), 531–554. https://doi.org/10.1175/jpo-d-17-0210.1

Soomere, T., Pindsoo, K., Kudryavtseva, N., & Eelsalu, M. (2020). Variability of distributions of wave set-up heights along a shoreline with complicated geometry. *Ocean Science*, *16*(5), 1047–1065. Retrieved from https://os.copernicus.org/articles/16/1047/2020/doi:10.5194/os-16-1047-2020

Stastna, M., & Legare, S. (2024). Simulations of shoaling large-amplitude internal waves: Perspectives and outlook. *Flowline*, *4*, E11. https://doi.org/10.1017/flo.2024.9

Turkington, B., Eydeland, A., & Wang, S. (1991). A computational method for solitary internal waves in a continuously stratified fluid. *Studies in Applied Mathematics*, *85*(2), 93–127. https://doi.org/10.1002/sapm199185293

Venayagamoorthy, S. K., & Fringer, O. B. (2012). Examining breaking internal waves on a shelf slope using numerical simulations. *Oceanography*.

Vieira, G. S., & Allshouse, M. R. (2020). Internal wave boluses as coherent structures in a continuously stratified fluid. *Journal of Fluid Mechanics*, *885*, A35. https://doi.org/10.1017/jfm.2019.993

Vlasenko, V., Brandt, P., & Rubino, A. (2000). Structure of large-amplitude internal solitary waves. *Journal of Physical Oceanography*, *30*(9), 2172–2185. https://doi.org/10.1175/1520-0485(2000)030<2172:solais>2.0.co;2

Vlasenko, V., & Stashchuk, N. (2007). Three-dimensional shoaling of large-amplitude internal waves. *Journal of Geophysical Research*, *112*(C11). https://doi.org/10.1029/2007jc004107

Wallace, B. C., & Wilkinson, D. L. (1988). Run-up of internal waves on a gentle slope in a two-layered system. *Journal of Fluid Mechanics*, *191*, 419–442. https://doi.org/10.1017/S0022112088001636

Walter, R. K., Stastna, M., Woodson, C. B., & Monismith, S. G. (2016). Observations of nonlinear internal waves at a persistent coastal upwelling front. *Continental Shelf Research*, *117*, 100–117. https://doi.org/10.1016/j.csr.2016.02.007

Walter, R. K., Woodson, C. B., Arthur, R. S., Fringer, O. B., & Monismith, S. G. (2012). Nearshore internal bores and turbulent mixing in southern monterey Bay. *Journal of Geophysical Research*, *117*(C7). https://doi.org/10.1029/2012jc008115

Winant, C. D. (1974). Internal surges in coastal waters. *Journal of Geophysical Research*, *79*(30), 4523–4526. https://doi.org/10.1029/jc079i030p04523

Woodson, C. (2018). The fate and impact of internal waves in nearshore ecosystems [Journal Article]. *Annual Review of Marine Science*, *10*(10), 421–441. https://doi.org/10.1146/annurev-marine-121916-063619

Xu, C., & Stastna, M. (2020). Instability and cross-boundary-layer transport by shoaling internal waves over realistic slopes. *Journal of Fluid Mechanics*, *895*, R6. https://doi.org/10.1017/jfm.2020.389

Yuan, C., & Wang, Z. (2022). On diffraction and oblique interactions of horizontally two-dimensional internal solitary waves. *Journal of Fluid Mechanics*, *936*, A20. https://doi.org/10.1017/jfm.2022.60